Superconductivity in thin films of the High Entropy Alloy $(\mathbf{TaNb})_x(\mathbf{HfZrTi})_{1-x}$

Natascha Winter

Bachelor Thesis Physics
Date: January 29, 2019

Department of Physics
University of Zurich

Supervisors:

Prof. Dr. Andreas Schilling
Dr. Xiafou Zhang

Acknowledgement

I would like to thank Prof. Dr. Andreas Schilling for giving me the chance to write this thesis in his group. Further, I would like to thank my supervisor Dr. Xiafou Zhang for helping me all the time. Also I would like to thank the University of Zurich, especially the Physics department, for the interesting Bachelor courses and thesis. Secondly, I would like to thank my family and friends for the inspiration and support doing this thesis and the whole bachelor degree. Especially I would like to thank Simon J. for helping me if I had some troubles doing the data analyses with python.

Abstract

In this thesis, I have performed detailed transport measurements based on a series of high entropy alloy $(TaNb)_x(HfZrTi)_{1-x}$ thin films. We expected to find the most optional composition for further applications. By measuring the superconducting transitions in various magnetic field, we have determined the composition dependence of the superconducting parameters such as the transition temperature, the upper critical field, the penetration depth, the coherence lengths and some more. As result the highest transition temperature was obtained with $x = 0.5$ whereas the highest upper critical field was found at $x = 0.3$. Considering these films can be deposited at room temperature in very large scales and are quite robust as high entropy alloys, they are perfectly suitable for superconducting devices in harsh environments, such as superconducting nanowire single-photon detectors.

Abstract German

In dieser Arbeit habe ich elektrische Transportmessungen an dünnen Filmen der Hoch-Entropie Lebierung $(TaNb)_x(HfZrTi)_{1-x}$ durchgeführt mit dem Ziel die optimale Zusammensetzung für verschiedene Anwendungen zu finden. Dazu wurde der Übergang in den supraleitenden Zustand in verschiedenen Magnetfeldern gemessen. Aus diesen Resultaten konnte ich die verschiedenen supraleitenden Parameter wie die magnetische Eindringtiefe, die Kohärenzlänge, das oberes kritisches Feld und einige mehr abhängig von der Zusammensetzung berechnen. Die höchste kritische Temperatur wurde für die Komposition mit $x = 0.5$ gemessen, das höchste obere kritische Feld hingegen wurde bei $x = 0.3$ gefunden. Da diese Filme bei Raumtemperatur in vergleichsweise grossen Massstab herrgestellt werden und als Hoch-Entropie Legierung ziemlich robust sind, können sie sehr gut für supraleitende Komponenten unter schwierigen Bedingungen, wie z.B. in einem "Superconducting nanowire single-photon detector" kurz SNSPD, eingesetzt werden.

Contents

1 Introduction

Superconductivity is an interesting phenomena in physics which is still not completely understood. Its phenomenology in the superconducting phase (below a certain transition temperature) consists of two parts: First, the resistivity of the material is exactly zero, second, the magnetic field is expelled from the bulk of the material (Type I) or channelled into thin flux tubes (Type II) called the Meissner-Effect.
There are different kinds of superconductor conventional ones with quite low transition temperatures, which can be described within BSC theory, and unconventional ones, e.g. high-temperature superconductors as cuprates, with much higher transition temperature, which are not yet understood completely.
In this thesis thin films of $(TaNb)_x(HfZrTi)_{1-x}$ which is a so called High Entropy Alloy are analysed. They have quite a low transition temperature around 7K. The interesting thing about this material is that the superconductivity is very robust. Jing Guo et al. [1] recently reported in a paper that this compound is superconducting in the whole range of pressure from 0Pa up to 190GPa. For higher pressures the limitation was the break down of the crystal structure of the high entropy alloy which makes it interesting to examine thin amorphous films to try to avoid this problem. Nowadays, often Niobium-Titanium alloys are used for superconducting magnets for example in MRI devices. So the recently discovered superconductivity in the high entropy alloy $(TaNb)_x(HfZrTi)_{1-x}$ is of some interest to be further examined. Especially after the discovery of the very robust superconductivity against high pressure.
As first experiments on these thin amorphous films the resistivity was measured for different magnetic fields between 1.9K and 10K. With these results the transition temperature, upper critical field, coherence length, penetration depth, energy gap, diffusion constant, density of states at Fermi level and the Ginzburg Landau parameter were determined. Afterwards the results will be studied to find some trends for the composition with the most stable superconducting state.

2 Theory

2.1 High-entropy alloys

2.1.1 Definition

An alloy is sometimes described as a "mixture of metals" [2] which is not always the case. In general, an alloy is a mixture of a principal element (a metal with a concentration of up to 90% or more) with one or more other chemical elements that do not have to be metals. In contrast a high-entropy alloy [3] is a mixture of 5 or more principal elements which all have a concentration between 5% and 35% and possibly some minor elements with concentrations below 5%.
The principle behind these alloys is to maximize their mixing entropy as in solid phases thereby also the stability is enhanced with respect to the metallic compounds. From thermodynamics the mixing entropy (i.e. the entropy of the high entropy alloy with respect to the pure elements) for one mole can be calculated:

$$\Delta S_{conf} = -R \sum_{i=1}^{n} X_i \ln(X_i) \tag{2.1}$$

where X_i is the molar fraction of the ith compound. The highest entropy and thereby the highest stability is reached with an equiatomic alloy. As illustrated in Figure 1 the atoms in a HEA are randomly arranged on a crystal lattice. The crystal structures are often simple ones, such as BCC but have some lattice distortions, as the atoms with different sizes are randomly put on the lattice points. This can then cause different strains between the atoms.

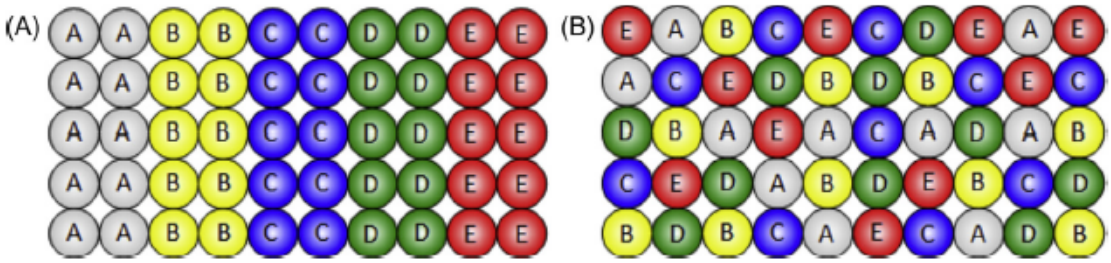

Figure 1: Five component high entropy alloy with similar atom sizes in equiatomic ratio. Figure (A) shows an ordered alloy with five parts all consisting of one kind of atom and (B) shows the high entropy alloy with atoms put randomly on the lattice.

High entropy alloys are quite a new discovery, first experiments were done in the early 2000's. They seem to have several interesting properties and have therefore often been examined during the last years. The properties of an alloy arise from the interaction between the constituents and have therefore first to be examined. Further, they also have some highly tunable properties that make them interesting for applications. There

are thousands of possibility to construct such high entropy alloys among which we find many superconductors.

The high-entropy alloy examined in this paper consists of five different elements: Niobium, Tantalum, Titanium, Zirconium and Hafnium. The concentration considered will be of the form: $(\mathrm{TaNb})_x(\mathrm{HfZrTi})_{1-x}$. All five elements are conventional superconductors (so they are described by BCS) and type I, except from Niobium which is type II, with different transition temperatures [4, 5]:

- Niobium: $T_c \approx 9.3\mathrm{K}$, type II superconductor
- Tantalum: $T_c \approx 4.5\mathrm{K}$, type I superconductor
- Titanium: $T_c \approx 0.4\mathrm{K}$, type I superconductor
- Zirconium: $T_c \approx 0.2\mathrm{K}$, type I superconductor
- Hafnium: $T_c \approx 0.5\mathrm{K}$, type I superconductor

2.1.2 Properties of $(\mathbf{TaNb})_x(\mathbf{HfZrTi})_{1-x}$

The superconductivity in this alloy was first examined in 2014 in a paper by P. Koželj et al. [6]. They did some transport measurement on the alloy $\mathrm{Ta_{34}Nb_{33}Hf_8Zr_{14}Ti_{11}}$ and found a transition temperature of $T_c = 7.3\mathrm{K}$.
Later, Fabian von Rohr et al. [7] further examined the alloy on a BCC lattice and found that it shows properties of simple crystalline intermetallics as well as the ones of amorphous materials.
Afterwards, Jing Guo et al. [1] did some further measurements on this alloy. They used the composition $(\mathrm{TaNb})_{0.67}(\mathrm{HfZrTi})_{0.33}$ and found that the superconducting state is very robust against pressure. The transition temperature at ambient pressure was around 7.8K, increased up to 10K at around 60GPa and was still around 9K at 190.6GPa which is comparable with the pressure of the outer core of the earth. For higher pressure it could not be examined if the HEA is still superconducting as the crystal was broken above this pressure. So it is not known if the superconductivity would be even more robust. This behaviour of a superconductor is quite unusual and is assumed to occur because of the stable crystal structure of this high entropy alloy.

2.2 Superconductivity

The phenomenology and theory about superconductivity are summarized from the following books and lecture notes: [8, 9, 10, 11, 12, 13]

2.2.1 Phenomenology of the superconducting phase

There exist two different types of superconductors:

- Type I superconductors: These are quite well understood nowadays and fully described by the BCS-theory. Typical examples are most of the elementary elements that are superconducting, as Tantalum.
- Type II superconductors: This type is still not fully understood as most of them are unconventional and contains most of the high temperature superconductors, as cuprates. Other examples are alloys or hight entropy alloys as discussed in this paper.

As the high entropy alloy $(\mathrm{TaNb})_x(\mathrm{HfZrTi})_{1-x}$ is a type II superconductor, the theory will mainly concentrate on this type.

Critical temperature

The critical temperature T_c is the most widely known critical point of the superconductor below which the sample enters the superconducting phase. In this phase two main effects occur:

i) the resistance immediately drops to 0Ω

ii) the magnetic field is fully expelled from the bulk in type I superconductors called Messner-Ochsenfeld effect or tunnelled into thin flux tubes and thus going into a vortex phase in type II superconductors

Both of these properties are reversible. But the transition temperature is not the only critical point in a phase diagram of a superconductor. They further have a critical magnetic field and a critical current.

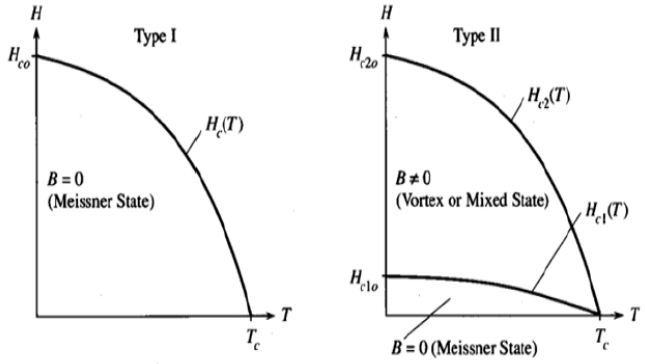

Figure 2: A typical phase diagram for a type I (left) and type II (right) superconductor [14]

Critical magnetic field

The superconducting transition temperature not only depends on the material but also on the magnetic field which is applied. By applying higher magnetic fields H to the superconductor the critical temperature is lowered. But if the field gets stronger, it will overcome the critical field ($H > H_{crit}$). Thereby the material will no longer be superconducting and undergoes a transition to a normal metallic or insulating state. As above also the superconducting state is reversible, hence by lowering the magnetic field, the material will re-enter the superconducting phase.

Meissner-Ochsenfeld effect and vortex phase

Now we have to distinguish between type I and type II superconductors. They have different phase diagrams as shown in Figure 2.

First we have a look at the effect in type I superconductors if they are placed in magnetic fields H, called the Meissner-Ochsenfeld effect. At room temperature, in the normal state, the magnetic field enters the superconductor (Figure 3). If the temperature is lowered below T_c at the transition, the magnetic field outside the sample changes abruptly and inside the superconductor it is equal to zero, so the material is in the Meissner state. By enhancing the magnetic field above the critical field H_c, it can penetrate through the sample and the superconducting state is destroyed. Again this process is reversible, that means by lowering the magnetic field the sample returns into the Meissner state and is superconducting again.

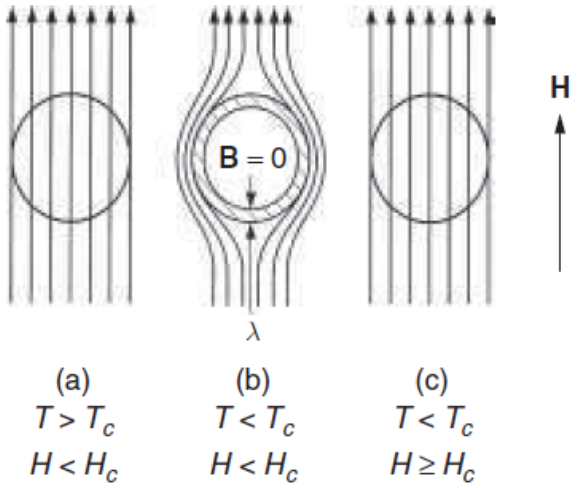

Figure 3: Illustration of the Meissner effect. In (a) the situation above T_c where the field penetrates the sample, (b) shows the superconducting state with zero field inside the superconductor and (c) the state above the critical field where the field again enters the superconductor.

This implies that in the superconducting phase, the sample is except from being a perfect conductor also a perfect diamagnet, which can be seen by looking at the susceptibility. The magnetic field inside the sample is equal to zero: $B = \mu_0(H + M) = 0$. Hence the magnetisation is minus the magnetic field: $M = -H$. Looking at the susceptibility: $\chi = M/H = -1$, we see the property of a perfect diamagnet.
However, this is not completely the case. The magnetic field can actually penetrate the sample over a small distance, called the penetration depth λ. In thick samples where $\lambda << d$ this does not matter but for thin films where probably $\lambda > d$ the Meissner effect cannot be observed: We will have a closer look at this in the next section.

For the type II superconductors we have a slightly different behaviour when applying magnetic fields. As in type II superconductors also these first enter the Meissner state but above a lower critical field H_{c_1} the sample enters the vortex phase. This means that the magnetic field inside the samples is tunnelled into thin flux tubes (Figure 4).
So in this case, applying a magnetic it will not be fully expelled from the bulk but above the lower critical field H_{c_1}, the first vortex will enter the superconductor and tunnel through. By enhancing the magnetic field towards the upper critical field H_{c_2}, the number of vortices increases. At the moment when the upper critical field is reached, the magnetic field will normally enter the sample and the superconducting phase is destroyed. As before, lowering the magnetic field will reconstruct the superconducting phase with the vortices.

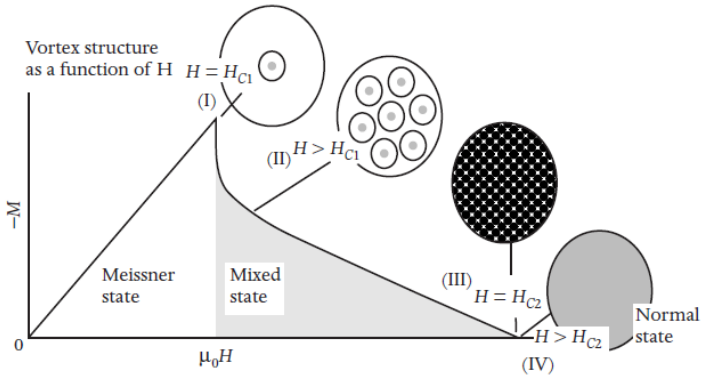

Figure 4: Illustration of the vortex phase depending on the magnetic field strength

Critical current

A different critical quantity is the critical current I_c of the superconductor, which is closely related to the critical field H_c. Applying a current on a superconducting sample will always produce a self-induced magnetic field. Increasing the current this self-induced field will be higher than the critical field and the superconducting state is destroyed.
If, in addition, the superconductor is placed in an external field, this critical current will be lower because the sum of the external and the self-induced field has to be smaller than the critical field. But we can circumvent this problem by taking alloys whose critical

current is determined by the lattice and homogeneities that will allow to create stronger superconductor magnets.

2.2.2 Theoretical aspects

Long time after the discovery of superconductivity in some materials a first microscopic theory about this phenomena was found by Bardeen, Cooper and Schrieffer. At low temperature, there occurs an attractive force between electrons which overcomes the repulsive Coulomb interaction and two electrons condensate to a Cooper pair. These Cooper pairs are bosonic in behaviour and can therefore go to lower energy. This can sometimes lead to a macroscopic occupation of a single state what would clearly contradict the Pauli Principle.

BCS theory

The Bardeen–Cooper–Schrieffer [15] theory (short BCS theory) can be applied to so called conventional superconductors but can be generalized to also be applicable to unconventional superconductivity.

This theory is based on the building of electron-electron pairs, so called Cooper-pairs. These pairs can only exist if there is an effective attraction between them, which means that except from the Coulomb repulsion there has to be an attractive force. In the standard BCS, i.e. for conventional superconductors, this force is mediated by the phonons. To understand this attractive force we consider a lattice with one ion on each lattice site and two electrons in this lattice. The ions are not fixed at the lattice point but can be deflected from the equilibrium position or oscillate. Because of the negative charge of the electron, the nearby ions will be attracted and an island of positive charge will occur as shown in Figure 5.

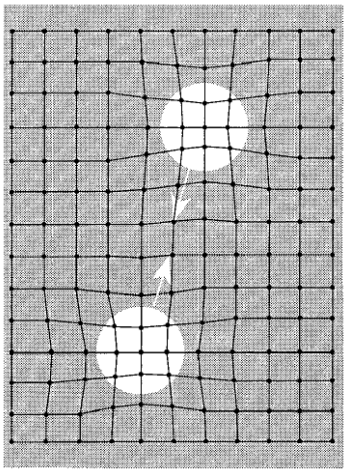

Figure 5: Polarisation of the lattice for attractive interaction between Cooper pairs

This positive polarisation of the lattice will attract the negatively charged second electron and vice versa. So the electrons seem to attract each other. Nevertheless, this process works only at sufficiently low velocity of the electrons, otherwise, the lattice cannot be polarized over a long enough time scale to attract the second electron, which is also the reason for low transition temperatures and non superconducting materials. Further, also the masses of the ions have an influence on the polarization of the lattice. For heavier ions the polarization is smaller what results a lower transition temperature. All these explanations are only qualitative and cannot be used for quantitative calculations.

These Cooper pairs are only built as their formation lowers the ground state energy of the material. If we again look at our first electron now travelling through the lattice, it will have left behind a deformation of the lattice. Now, there are two possibilities how the second electron can propagate inside the polarized field, lowering the energy of the system. Either it can follow, which would imply that both of them have the same momentum $\boldsymbol{p} = \hbar\boldsymbol{k}$. This superposition can then be seen as a new particle, called an electron pair with momentum $2\boldsymbol{p}$. Or the second possibility, they will build a Cooper pair where the second electron has opposite momentum $\boldsymbol{p_1} = -\boldsymbol{p_2}$. In this case the total momentum of this quasiparticle will be $\boldsymbol{p} = 0$. The two electrons in the Cooper pair must have different spin polarisations (to ensure that the wavefuction of the Cooper pair is antisymmetric) and can therefore be written as $\{\boldsymbol{k}\uparrow, -\boldsymbol{k}\downarrow\}$. More general, if the Cooper pair is not static as in the ground state $T = 0K$ but moving in the lattice, i.e. conducting, it will have the form:

$$\{\boldsymbol{k} + \boldsymbol{K}\uparrow, -\boldsymbol{k} + \boldsymbol{K}\downarrow\} \tag{2.2}$$

As we can see, this pair has then a total spin of $S = 0$, so it follows the Bose-Einstein statistic and does not obey the Pauli-Principle as single electrons would. We have already seen that these Cooper pairs can only exist at low enough energies where the attractive phonon-electron interaction overcomes the repulsive electron-electron interaction. A further limitation is the BSC-coherence length ξ_0 which is a measure for the mean expansion of a Cooper pair and also defines the distance over which Cooper pairs can be built. Further, Cooper-pairs only exist near the Fermi surface in a small energy range $\hbar\omega$.

The formation of Cooper pairs opens a gap Δ in the energy dispersion which makes the superconducting state energetically favourable (Figure 6). To excite a Cooper pair into a quasiparticle above this gap at least an energy of 2Δ is needed. But they can also be broken by thermal excitation and as the density of Cooper pairs n_s is proportional to Δ^2 we know that for $T \to T_c$ we have $\Delta \to 0$.

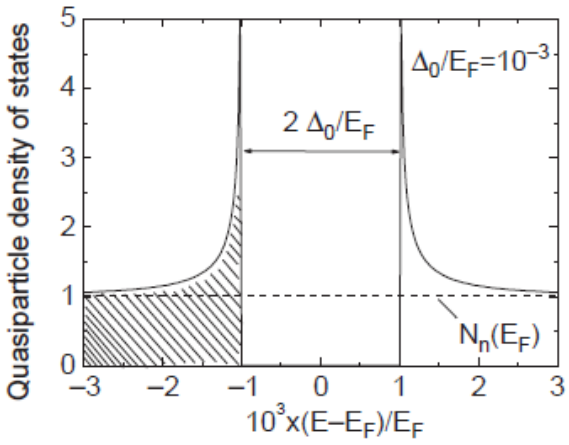

Figure 6: Gap in the normalized density of states of the quasiparticles in a superconductor

Within BCS-Theory we find a simple formula for the transition temperature:

$$T_c = 1.13\frac{\hbar\omega_D}{k_B}\exp\left(-\frac{1}{N_n(\epsilon_F V)}\right) \tag{2.3}$$

As the Debye frequency depends on the mass, one also finds that the lower the mass, the higher the transition temperature can get. The second great result from the BCS theory is the relation between the gap at zero temperature and the transition temperature:

$$2\Delta(T=0) = 3.5 k_B T_c \tag{2.4}$$

Cooper pairs can also occur above T_c because of thermal fluctuations but they only exist over a short time and localized. So there are short superconducting islands that enhance the conductivity but cannot turn the material superconducting.

All this was about conventional superconductors. If we now want to turn to unconventional ones, the main difference is that the attractive interactions do not come from the phonon-electron interaction but are mediated in a different way. This leads to a k dependent gap with nodes at some points or lines where the gap is closed.

London Theory

By looking at a superconductor as a macroscopic system one can actually show the perfect diamagnetism using the equation of motion of en electron with mass m, velocity $\boldsymbol{v}$ and charge e in an electrical field which reads $m\dot{\boldsymbol{v}} = e\boldsymbol{E}$. With the number density n of electrons one can write the current density as $\boldsymbol{J} = ne\boldsymbol{v}$. Combining these, we can find an equation for the electrical field $\boldsymbol{E} = \frac{m}{ne^2}\dot{\boldsymbol{J}}$. Using the two Maxwell equations:

$$\nabla \times \boldsymbol{E} = -\frac{\partial \boldsymbol{B}}{\partial t} \tag{2.5}$$

$$\nabla \times \boldsymbol{B} = \mu_0 \boldsymbol{J} \tag{2.6}$$

one finds the differential equation:

$$\nabla^2 \dot{\boldsymbol{B}} = \frac{ne^2\mu_0}{m}\dot{\boldsymbol{B}} = \frac{1}{\lambda^2}\dot{\boldsymbol{B}} \tag{2.7}$$

where we have defined the London penetration depth as $\lambda^2 = \frac{m}{ne^2\mu_0}$ having dimension of a length. The solution of this equation is then given by:

$$\dot{\boldsymbol{B}}(x) = \dot{\boldsymbol{B}}(0)\exp\left(-\frac{x}{\lambda}\right) \tag{2.8}$$

So our λ can clearly be seen as the depth inside the superconductor where the magnetic field can change. For $x >> \lambda$ this equation will result in $\dot{\boldsymbol{B}}(x) = 0$ which means that inside the superconductor the magnetic field is constant. The phenomenological Meissner effect would imply that it is constant equal to zero. Therefore, London stated that superconductivity arises from superelectrons with density n_s and found the following two equations known as the London equations:

$$\boldsymbol{E} = \mu_0\lambda_s^2\dot{\boldsymbol{J}} \tag{2.9}$$

$$\mu_0\lambda_s^2\nabla\times\boldsymbol{J} + \boldsymbol{B} = 0 \tag{2.10}$$

The first London equation 2.9 which is the same as the equation of motion for a perfect conductor and the second London equation 2.10. Using $\boldsymbol{B} = \nabla\times\boldsymbol{A}$ in the gauge where $\nabla\cdot\boldsymbol{A} = 0$ this leads to $\mu_0\lambda_s^2\boldsymbol{J} + \boldsymbol{A} = 0$. In the same way as above using the Maxwell equation one arrives at:

$$\nabla^2\boldsymbol{B} = \frac{1}{\lambda_s^2}\boldsymbol{B} \tag{2.11}$$

with the solution:

$$\boldsymbol{B}(x) = \boldsymbol{B}(0)\exp\left(-\frac{1}{\lambda_s}\right) \tag{2.12}$$

where λ_s is defined as

$$\lambda_s^2 = \frac{m^*}{n_s e^{*2}\mu_0}\,. \tag{2.13}$$

where the star indicates the renormalized mass and charge of the superelectrons. This result exactly explains the Meissner effect that for $x >> \lambda$ the magnetic field inside the superconductor is zero with an additional fact that inside the penetration depth $x < \lambda$ the field can enter the superconductor but will decay exponentially as shown in Figure 7.

The experimental measured temperature dependence of the penetration depth can be approximated by:

$$\lambda(T) = \lambda(0)\left[1 - \left(\frac{T}{T_c}\right)^4\right]^{-1/2} \tag{2.14}$$

Within the BCS theory the following formula was found:

$$\lambda(T) = \lambda(0)\left[\frac{\Delta(T)\tanh\left(\frac{\Delta(T)}{2k_BT}\right)}{\Delta(0)}\right]^{1/3} \tag{2.15}$$

which actually describes the dependence more exactly. Near T_c both formula represent the same behaviour:

$$\lambda(T) = \lambda(0)\left[2\left(1 - \frac{T}{T_c}\right)\right]^{-1/2} \tag{2.16}$$

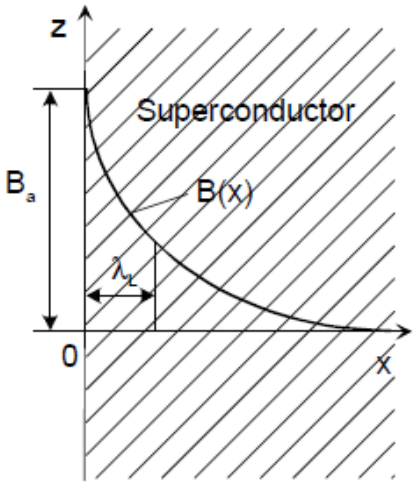

Figure 7: Decay of the magnetic field inside a superconductor and London penetration depth

Further, from the penetration depth also the critical current can be determined, above it, the superconducting state will be destroyed. By differentiating the formula for the magnetic field inside the sample with respect to x we obtain:

$$J(x) = \frac{dH}{dx} = \frac{dB}{dx}\frac{1}{\mu_0} = -\frac{B(0)}{\lambda\mu_0}\exp\left(-\frac{1}{\lambda_s}\right) \tag{2.17}$$

Inserting for the magnetic field $B(0)$ the critical magnetic field one obtains $J_c = \frac{H_c}{\mu_0\lambda}$ for the maximal current at the surface $x = 0$. For values $J > J_c$ all Cooper pairs are broken and superconductivity is destroyed.

Ginzburg-Landau Theory

The Ginzburg-Landau also known as GLAG (Ginzburg Landau Abrikosov Gor'kov) theory is based on the property that the superconducting phase is a well defined thermodynamic phase with the order parameter $\Psi(\boldsymbol{r})$ increasing from zero at T_c up to one at $T = 0$. We can interpret $|\Psi(\boldsymbol{r})|^2$ as the density of superconducting electrons. The phase transition to the superconducting state at $T = T_c$ is a second order transition which is described by the theory of Landau.

We consider the Gibbs free energy g_s of the superconducting state in zero magnetic field and expand it as a Taylor series in $|\Psi(\boldsymbol{r})|^2$: $g_s = g_n + \alpha|\Psi(\boldsymbol{r})|^2 + \frac{1}{2}\beta|\Psi(\boldsymbol{r})|^4 + \dots$ where g_n is the free energy in the normal state. We want to minimize this function to get a state that is stable (as the superconducting state), therefore we can already make some assumptions:

i) Keeping in mind that the system will be in the state with the lowest energy we know g_s must be smaller than g_n for $T < T_c$ but $g_s > g_n$ for $T > T_c$.

ii) The parameter β needs to be positive, otherwise, for very large value of the order parameter Ψ we would get the lowest energy and minimization of the energy would lead to $\Psi \to \infty$ and give a superconducting state also above T_c.

iii) For $T < T_c$ the parameter α must be negative to make the free energy smaller in the superconducting state with higher order compared to the normal state energy.

iv) For $T > T_c$ we want the superconducting free energy to be higher than the one in the normal state and further, we also want the state with zero order to be the most favourable. Therefore we need α to be positive in this regime.

Considering these assumptions we can expand the parameters α and β to first order in temperature:

$$\alpha(T) = \alpha(0)\left(\frac{T}{T_c} - 1\right) \tag{2.18}$$

$$\beta(T) = \beta = \text{const.} \tag{2.19}$$

If we want to find the equilibrium value of the order parameter Ψ_{inf} s.t. $n_s = |\Psi_{\text{inf}}|^2$, we need to minimize the free energy with respect to the order parameter:

$$\frac{dg_s}{d|\Psi|^2} = 0 \quad \Longleftrightarrow \quad \alpha + \beta|\Psi_{\text{inf}}|^2 = 0 \tag{2.20}$$

With this we obtain:

$$n_s = |\Psi_{\text{inf}}|^2 = -\frac{\alpha(T)}{\beta(T)} = \frac{\alpha(0)}{2\beta(0)}\left(1 - \frac{T}{T_c}\right) \tag{2.21}$$

Inserting this into the free energy we get:

$$g_s - g_n = -\frac{1}{2}\frac{\alpha^2(T)}{\beta(T)} = -\frac{\alpha^2(0)}{2\beta T_c^2}(T - T_c)^2 \tag{2.22}$$

We can now also consider spatial variations of the order parameter and the influence of a magnetic field, then we have for the Gibbs free energy:

$$g_s(B) = g_n + \alpha|\Psi|^2 + \frac{1}{2}\beta|\Psi|^4 + \frac{1}{2\mu_0}|\boldsymbol{B_a} - \boldsymbol{B_i}|^2 + \frac{1}{2m^*}\left|\left(\frac{\hbar}{i}\nabla - q\boldsymbol{A}\right)\Psi\right|^2 \tag{2.23}$$

This formula contains two additional terms, the first one referring to the energy needed to change the magnetic field and the second for the spatial variations of the order parameter. To get the total energy we need to integrate this term over the volume: $G_s(B) = \int_V g_s(B)dV$. Minimizing this function by variation of Ψ and $\boldsymbol{A}$ leads to the following two Ginzburg-Landau equations:

$$\frac{1}{2m^*}\left(\frac{\hbar}{i}\nabla - q\boldsymbol{A}\right)^2 \Psi + \alpha\Psi + \beta|\Psi|^2\Psi = 0 \tag{2.24}$$

$$\boldsymbol{j_s} = \frac{q\hbar}{2m^*i}(\Psi^*\nabla\Psi - \Psi\nabla\Psi^*) - \frac{q^2}{m^*}|\Psi|^2\boldsymbol{A} \tag{2.25}$$

Using equation 2.25, the definition of the London penetration depth $\lambda_L^2 = \frac{m^*}{\mu_0 q^2 n_s}$ and giving the order parameter a phase $\psi = \frac{\Psi}{\Psi_{\text{inf}}} = \psi_0 e^{i\varphi}$ we arrive at $\boldsymbol{j_s} = -\frac{1}{\mu_0\lambda_L^2}\boldsymbol{A}$. By taking the curl on both sides this results in the London equation (2.10):

$$\boldsymbol{B} = -\mu_0\lambda_L^2\nabla\times\boldsymbol{j_s} \tag{2.26}$$

Considering the first Ginzburg-Landau equation 2.24 taking again $\psi = \frac{\Psi}{\Psi_{\text{inf}}}$ and the fact that $n_s = |\Psi_{\text{inf}}|^2 = -\frac{\alpha}{\beta}$ we find that:

$$-\xi_{GL}^2\left(\frac{1}{i}\nabla - \frac{q}{\hbar}\boldsymbol{A}\right)^2\psi + \psi - |\psi|^2\psi = 0 \tag{2.27}$$

where we have defined $\xi_{GL}^2 = -\frac{\hbar}{2m\alpha}$ the Ginzburg-Landau coherence length. To get an understanding of this length we assume a superconductor with infinite dimension in y and z and starting at $x = 0$ extended to $x \to \infty$ in zero magnetic field $\xi_{GL}^2\frac{d^2\psi}{dx^2} + \psi - \psi^3 = 0$ with the solution for $x > 0$:

$$\psi(x) = \tanh\left(\frac{x}{\sqrt{2}\xi_{GL}}\right) \tag{2.28}$$

shown in Figure 8.

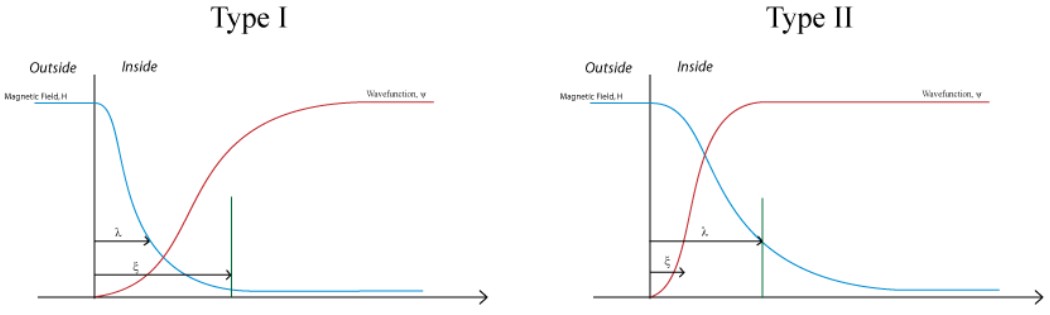

Figure 8: Relation between coherence length and penetration depth inside a type I and type II superconductor [16]

As shown in Figure 8 the order parameter first increases more or less linearly from 0 to nearly 1 and then saturates until infinity at 1. This leads to the interpretation of ξ_{GL} as the minimal length to change the order parameter Ψ to 0.

To end this section we want to consider the temperature dependence of these two lengths. As both λ_L and ξ_{GL} depend on α we can find the temperature dependence of both but need to keep in mind that the Ginzburg-Landau theory is only valid for $T \to T_c$ although they include their values at zero temperature.

$$\lambda_L(T) = \frac{\lambda_L(0)}{\sqrt{1 - T/T_c}} \qquad \xi_{GL}(T) = \frac{\xi_{GL}(0)}{\sqrt{1 - T/T_c}} \tag{2.29}$$

Looking at these equations we see that in the limit $T \to T_c$ (where they are properly defined) both diverge to infinity.

To summarize, we have now seen three characteristic lengths of a superconductor:

i) penetration depth λ_L which gives the distance over which magnetic fields decay inside a superconductor

ii) BSC coherence length $\xi_0 = 0.18\frac{\pi\hbar v_F}{2k_B T_c}$ which is the average extension of a Cooper pair

iii) Ginzburg-Landau coherence length ξ_{GL} which is a measure for the minimal distance needed to change the superconducting order parameter

Looking at the relation between these parameters we can deduce that $\xi_{GL} > \xi_0$ since the length needed to change the number of Cooper pairs surely has to be larger than the extension of these. An important relation to define is the Ginzburg-Landau parameter $\kappa = \frac{\lambda_L}{\xi_{GL}}$ which is independent of temperature and magnetic field and can therefore be used to classify superconductors (see Figure 8):

- if $\kappa < \frac{1}{\sqrt{2}}$ we have a type I superconductor
- if $\kappa \geq \frac{1}{\sqrt{2}}$ the superconductor is type II und will enter the vortex phase above a lower critical field H_{c_1}.

In a more phenomenological way, we can say that if the penetration of the magnetic field is larger than the length needed to change the order parameter, it is possible that thin flux tubes can enter the superconductor.
Within this theory it is also possible to calculate the critical field of a type I superconductor. Using thermodynamics one can add the magnetic part (coming from the magnetisation) to the Gibbs free energy $dG = -SdT + Vdp - mdB$ leading to:

$$G_s(B) = G_s(0) - \int_0^B m dB \tag{2.30}$$

As a system always chooses the state with lowest energy the critical field is at the point where $G_s(B) = G_n(B) = G_n(0)$.

The upper critical field of a type II superconductor (which is examined in this thesis) can be found by some qualitative considerations. Enhancing the magnetic field yields more and more flux tubes. Such a flux tube can only occur within a circle with minimal radius equal to the coherence length (since this length is needed to change the order parameter to zero). Considering a plane perpendicular to the magnetic field of area L^2. Superconductivity will break down if this area is completely filled with the flux tubes: $N2\pi\xi_{GL} = L^2$. The magnetic field will then be $B = \frac{N\phi_0}{L^2}$. Substituting one of these equations into the other yields:

$$B_{c_2} = \frac{\phi_0}{2\pi\xi_{GL}^2} \tag{2.31}$$

This formula can also be found taking again the Gibbs free energy. Further, the temperature dependence is given by the temperature dependence of the coherence length. With similarly simple considerations one can find an approximation for the lower critical field. The first flux tube will be able to enter the superconductor if the flux through the area of radius equal the penetration depth will be equal to the flux quantum: $\pi\lambda_L^2 B = \phi_0$. In this case the lower critical field would be: $B_{c_1} = \frac{\phi_0}{\pi\lambda_L^2}$. This is actually not the value found in literature but comparable. Starting with the Gibbs free energy the critical field is found to be:

$$B_{c_1} = \frac{\phi_0}{4\pi\lambda_L^2}\ln(\kappa - 0.08) \tag{2.32}$$

2.2.3 Amorphous superconductors

The superconductors examined in this experiment are amorphous films so they do not have any long range atomic order which means that the concept of phonons as crystalline quasiparticles cannot be applied (Figure 9). This also implies that they cannot be conventional superconductors as the positive attraction between two Cooper pairs cannot be mediated by phonons. In amorphous films [17] there only exists a short range order of the atoms but as in a crystal, the atoms can vibrate around their equilibrium position with different frequencies. This leads to very strong interactions between the conducting electrons and the atoms which result in an attractive interaction between the electrons and therefore the formation of superconducting Cooper Pairs.

In contrast to conventional superconductors, some important limitations can be found. Most importantly, concerning the coherence length and the penetration depth. As the attractive interaction is due to inelastic scattering, there is no phase coherence between the electrons and therefore the coherence length ξ is very short of the order of the mean free path (a few nanometer). The penetration depth is related to the normal state conductivity. Lower normal state conductivity implies a higher penetration depth and as amorphous films have lower normal state conductivity the penetration depth λ is increased. Taking these two properties together we have $\lambda >> \xi$. This leads to a very

high Ginzburg Landau Parameter κ and therefore to a strong type II superconductivity.

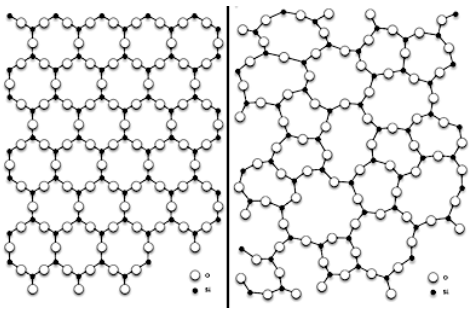

Figure 9: Comparison between the crystalline and the amorphous structure [18]. The crystalline order which has a defined lattice symmetry with unit cells on the left. On the right a typical amorphous crystal with only short range order is shown.

3 Experiment

To find the critical temperature T_c and further the upper critical field B_{c_2} transport measurements were done. Using the physical property measurement system (PPMS) the amorphous films were cooled down below the critical temperature, which is known to be around 7K in zero magnetic field, to observe the transition in the resistance. The PPMS is a cryostat with a magnet and can be used for transport measurements down to 1.8K in different magnetic fields.

3.1 Preparation of the films

For the preparation of the films the High Power Impulse Magnetron Sputtering (HiPIMS) [19, 20] was used. This device is often used to grow thin amorphous films on different substrates.
For the sputtering process two targets are placed on a magnetron. One containing Tantal and Niobium and the other one the three elements Hafnium, Zirconium and Titanium. The chamber used for the sputtering has first to be evacuated to create a vacuum. Afterwards, a process gas, in this case argon, is put into the chamber with a very low pressure. The magnetron is then used as the cathode and the chamber acts as the anode to accelerate electrons. These electrons collide with the argon atoms and ionize them. This positively charged ion is then accelerated towards the magnetron carrying enough energy to remove an atom of the target material which then will condensate on the substrate. The still ionized argon atoms recombine with the free electrons what creates a visible plasma. In the magnetron sputtering, in addition, a magnetic field is applied to get a better ionisation of the process gas. The HiPIMS involves a plasma with a much higher density such that the sputtering rate is increased. This is achieved by a much higher voltage applied on the magnetron. To reach the therefore needed high electrical power the voltage is pulsed with a low duty factor (which means most of the time the source is switched off) to be able to cool the system.

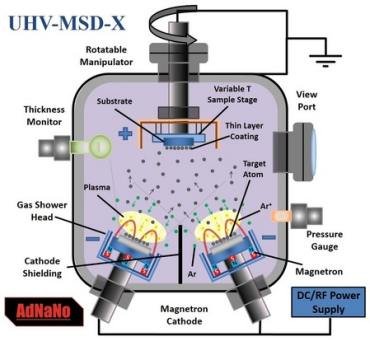

Figure 10: Schematics of a HiPIMS with high density plasmas [21]

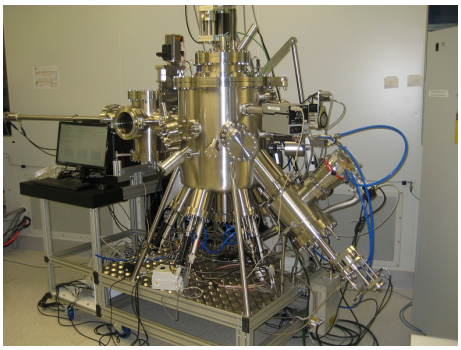

Figure 11: Picture of the HiPIMS from Mantis at ETH [22]

Varying the electric potential on the cathode and the deposition time, films with different compositions and thickness can be produced. For this thesis $(\mathrm{TaNb})_x(\mathrm{HfZrTi})_{1-x}$ films with x from 0.1 to 0.9 in steps of 0.1 were produced. All with a thickness of between 600nm and 1μm.

Afterwards, the thickness of the films was measured with a profilometer from *Dektat* [23]. This device scans the surface of the sample with a diamond pin, always being in contact with the sample. Like this the prifilometer can measure surface variation with a resolution of ~ 5Å. For the measurement of the film thickness not only the films but also the pure substrate around the films was scanned (Figure 12). By calibrating the height of the substrate to 0 (red shaped area), the thickness of the film can be read out directly from the green shaped area. The results of the measurements are summarized in Table 1.

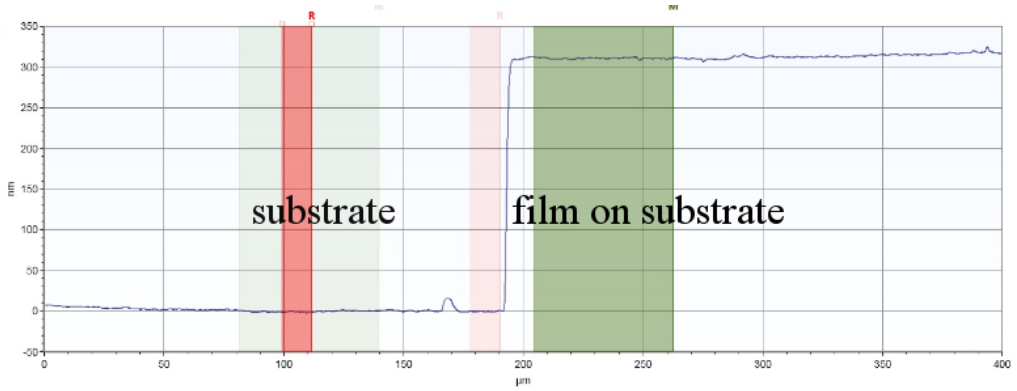

Figure 12: Output of the measurement of the film thickness. On the left side the surface of the substrate is scanned and on the right the surface of the film which is on the substrate.

The composition of the films was checked with the scanning electron microscope (SEM). In Figure 13, the peaks for the different elements in the film are clearly visible. From these the fraction of each element can be determined. In most cases the part of the target with TaNb was a bit larger than predicted which can be explained by a systematic error but it does not matter that much, as we only want to compare the compositions relative to each other.

composition x	0.1	0.2	0.3	0.4	0.5	0.6	0.7	0.8	0.9
thikness d [nm]	955	750	630	635	625	620	622	623	740

Table 1: Overview thickness of the different films

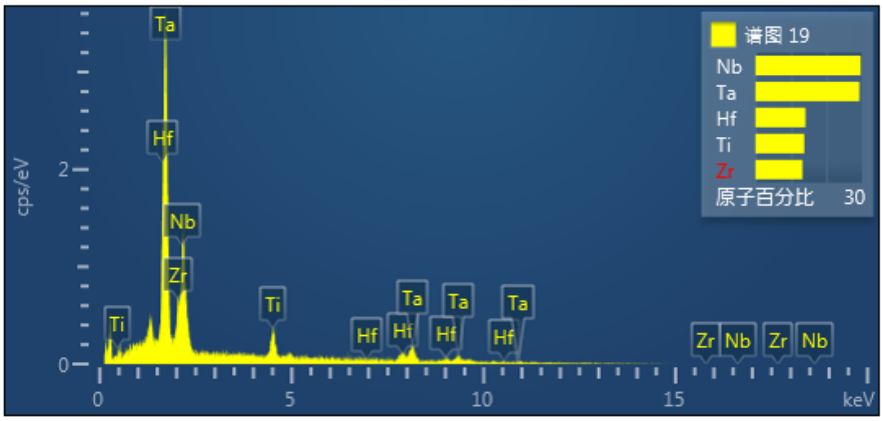

Figure 13: The composition of the different elements in the film using SEM. The Graph shows the peaks which ware labelled with the element they correspond to. On the intercept on the right the rates of each element are extracted from the graph. In this case: Nb 29.62%, Ta 29.27%, Hf 14.10%, Ti 13.76% and Zr 13.24%

3.2 Transport measurement

The transport measurements were done with a physical properties measurement system (PPMS) from *quantum design* [24, 25]. This device can be used for many different magnetic, electric and thermal measurements, as heat capacity, resistivity or magnetisation. It mainly consists of a helium cryostat that can be controlled by a "Model 6000" which allows to directly apply different voltages and currents. This process can further be automatized with a software on the computer where it is possible to program a whole sequence which then is executed by the system itself.
The temperature range goes from 1.9K (sometimes even 1.8K) up to around 400K. For the cooling down to 4.2K liquid helium can be used. Afterwards, the cooling process is continued by pumping the vaporized helium which further cools down the system. With a helium-3 refrigerator even temperatures down to 0.4K can be achieved.
On the other hand, the magnetic field can be controlled from 0T up to 9T or even up to 16T in other devices. This is done by a superconducting magnet.
Figure 14 is a picture of the PPMS and Figure 15 shows the schematic setup of the cryostat with all different isolations.
For transport measurements the sample holder is shown in Figure 16. It is possible to measure three samples at the same time all with a 4 point measurement. The advantage of this 4 point measurement is that the current and voltage are measured separately and the measurement of the one does not influence the other. So in this experiment by putting a certain current between two of the four wires, the voltage can be measured over the other ones without any connection to the current. This provides a much higher accuracy.

Figure 14: Picture of the PPMS from *Quantum Design* [26]

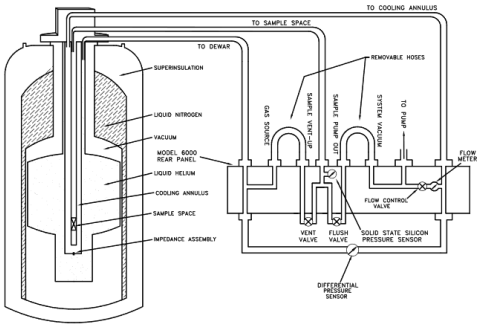

Figure 15: Schematic setup of the physical property measurement system [27]

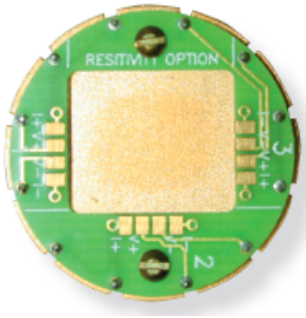

Figure 16: Sample holder for the transport measurement done with the physical property measurement system (i.e. the model 6000) [28]

Figure 17: Test box to put the sample holder used for the determination of the sheet resistance at room temperature [28]

3.3 Performance of the experiment

First, the prepared films in a more or less squared shape are put on the sample holder and are fixed with adhesive. Afterwards, the four contact wires between the contacts on the sample holder and the film were made with a *tpt* wire bonder. As material for the wire, gold was used to minimize the resistivity of the wires. This prepared sample was then put into the helium cryostat. To measure the resistance, a current was applied to the sample. This current has to be below the critical current of the superconducting state and was chosen to be between 100μA to 1mA depending on the composition of the films. From the resulting voltage on the other contacts then the resistance was automatically calculated by Ohm's law and saved. To get more reliable results, this resistance measurement was performed five times for each temperature and magnetic field.
In zero magnetic field in a first sequence the resistance was measured from 300K down to 1.8K (Figure 18). Knowing the transition temperature to be around 7K or below,

the measurement with applied magnetic field was only done from 10K or 8K down to 1.9K, respectively, to extract the transition temperature for different fields (Figure 19). During this sequence first the magnetic field was set, then, the system was cooled down, and afterwards, heated up again to reset the magnetic field and so on. The magnetic field was applied in steps of 0.2T in the range $0\mathrm{T}-2\mathrm{T}$ and then in steps of 0.5T up to 9T.

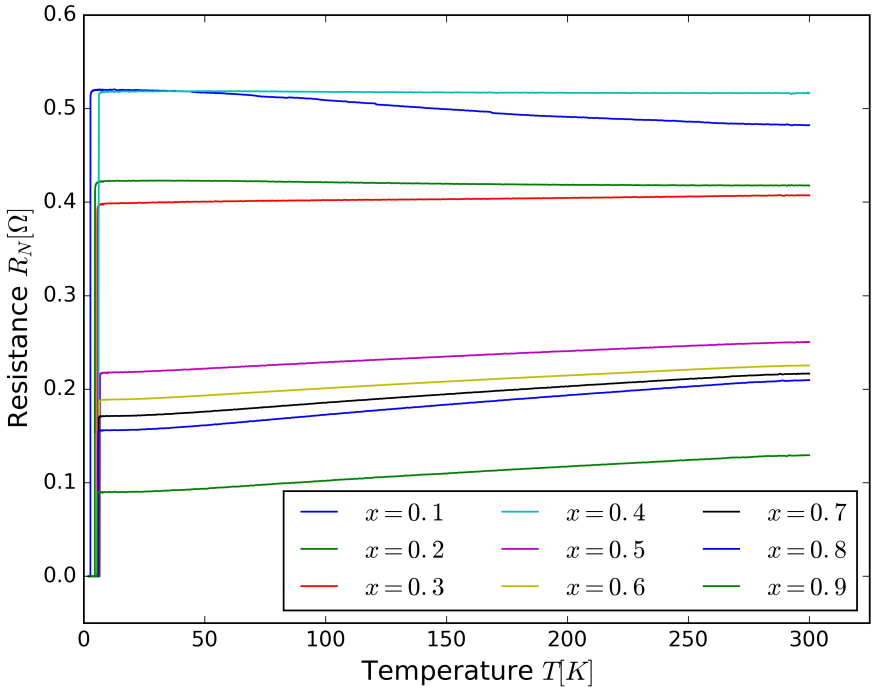

Figure 18: Plot of measured resistance for all different compositions from 300K to 1.8K. The strongly varying normal state resistance comes from the different shapes and thicknesses of the measured films.

As the thin films are not exactly square shaped the measured resistance is not equal the sheet resistance $R \neq R_S$ and therefore a second measurement was needed. This measurement was done at room temperature with a sample test box (Figure 17). For each film four measurements of the resulting voltage were done using a fixed current of 1A. Still having the four point wires on the sample the current was applied between any two neighbouring contacts measuring the voltage over the other two.

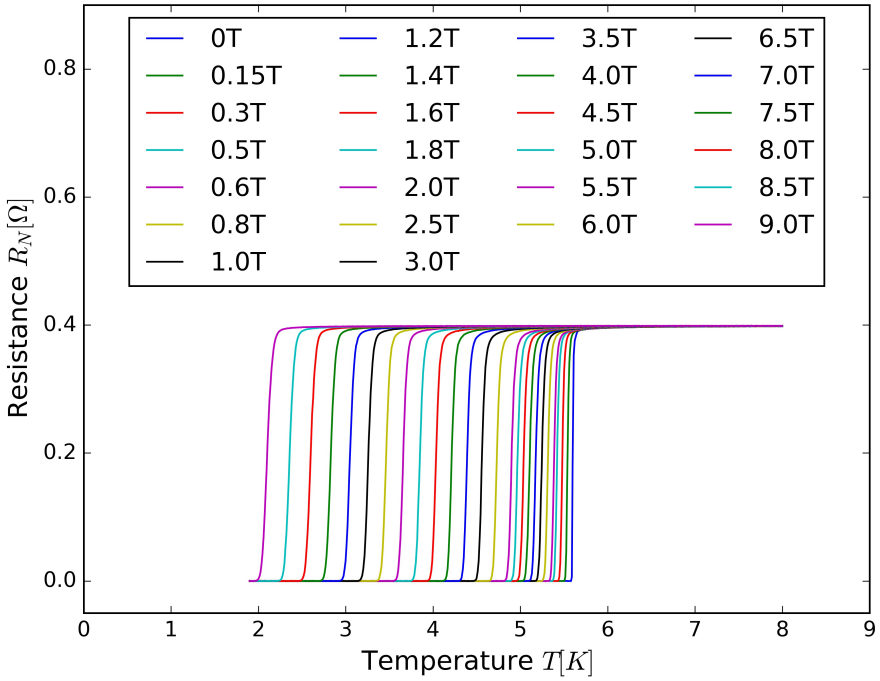

Figure 19: Plot of the measured resistance for the film with composition $x = 0.3$ in different magnetic fields. For higher magnetic fields than 5T there is no superconducting transition down to 1.9K. The plots for the other compositions look quite similar but the highest magnetic field still showing a transition varies depending on the composition.

3.4 Data

The overall received data for the analysis are:

- the film thicknesses from the measurements with the profilometer restored in Table 1
- the exact compositions from the measurement with the SEM but for the graphs nevertheless the calculated compositions were used
- the normal resistance of all compositions in zero magnetic field from 300K down to 1.8K and in different magnetic fields from 10K/8K down to 1.9K
- the measured voltage at room temperature between any neighbouring contacts on the films to calculate the correction between sheet resistance and measured normal resistance

This data was then analysed using python and excel to first get the resistivity out of the measured resistance and afterwards the different superconducting parameters as the transition temperature, upper critical magnetic field, etc. depending on the composition. All the data was received with a small statistical error ($< 1\%$) which is too small to be seen as error bars in the plots.

4 Results and Analysis

4.1 Resistivity

To get the resistivity out of the measured normal state resistance first the sheet resistance has to be found [29]. The resistance can be written as $R = \frac{\rho}{t}\frac{L}{W} = R_S\frac{L}{W}$ with t standing for the thickness of the film and L, W for the length and the width, respectively. In the second step, the sheet resistance was defined as $R_S = \frac{\rho}{t}$. As the films are not exactly rectangular shaped, i.e. L and W are not defined, the connection between the measured resistance and the sheet resistance has to be found in a different way using the four measurements of the voltage with fixed current.
The sheet resistance is then defined as [30]:

$$R_S = \frac{\pi}{8\ln(2)}\sum_{n=1}^{4}\left(\frac{V_n + V_{n+1}}{I}\right) f\left(\frac{V_{n+1}}{V_n}\right) \tag{4.1}$$

where the Van der Pauw function f can be found numerically from

$$\frac{\frac{V_{n+1}}{V_n} - 1}{\frac{V_{n+1}}{V_n} + 1} = \frac{\operatorname{arcosh}\left(\frac{\exp(\ln(2)/f)}{2}\right)}{\ln(2)/f} \tag{4.2}$$

Using this equation the sheet resistance at room temperature ($T = 294\text{K}$) was calculated for all compositions and compared to the measured resistance at the same temperature. As the correction factor between the measured resistance and the sheet resistance is temperature independent, it can be calculated at room temperature and be used for all temperatures. From the sheet resistance the electrical resistivity can be calculated as $\rho = R_S t$. Table 2 shows the measured resistance, sheet resistance, resistivity at room temperature and the correction factor for the different shapes $\frac{L}{W} = \frac{R_N}{R_S}$ for all films.

composition x	0.1	0.2	0.3	0.4	0.5	0.6	0.7	0.8	0.9
resistance $R_N[\Omega]$	0.483	0.418	0.407	0.517	0.250	0.225	0.216	0.209	0.129
sheet resistance $R_S[\Omega]$	1.490	1.594	1.632	1.432	1.210	1.000	0.849	0.628	0.483
resistivity $\rho[\mu\Omega\text{cm}]$	142.27	119.52	10.284	90.91	75.63	62.00	52.84	39.09	35.74
correction factor L/W	0.324	0.262	0.249	0.361	0.207	0.225	0.254	0.334	0.267

Table 2: Overview of the connection between the resistance, the sheet resistance and the resistivity depending on the composition

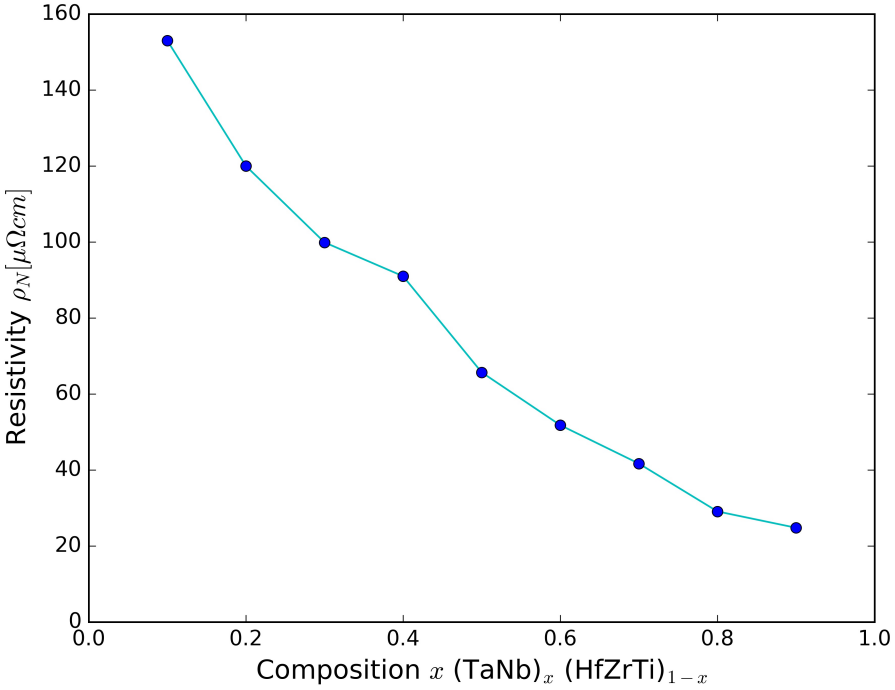

Figure 20: Normal state resistivity ρ_N plotted againtst the composition of the films. The dots are the determined resistivities, the line is inserted to show the linear trend of this quantity.

The resistivity determined just above the superconducting transition was read out and plotted for the different compositions in Figure 20. It shows quite a linear behaviour which gives higher resistivity the more of HfZrTi is included, i.e. the lower x (part of TaNb) is. This was also expected if one looks at the resistivity of the pure films (Figure 21) where TaNb seems to turn superconducting a bit below 1.9K, whereas on the other hand in HfZrTi, the resistivity again increases just around 1.9K after dropping nearly to zero.

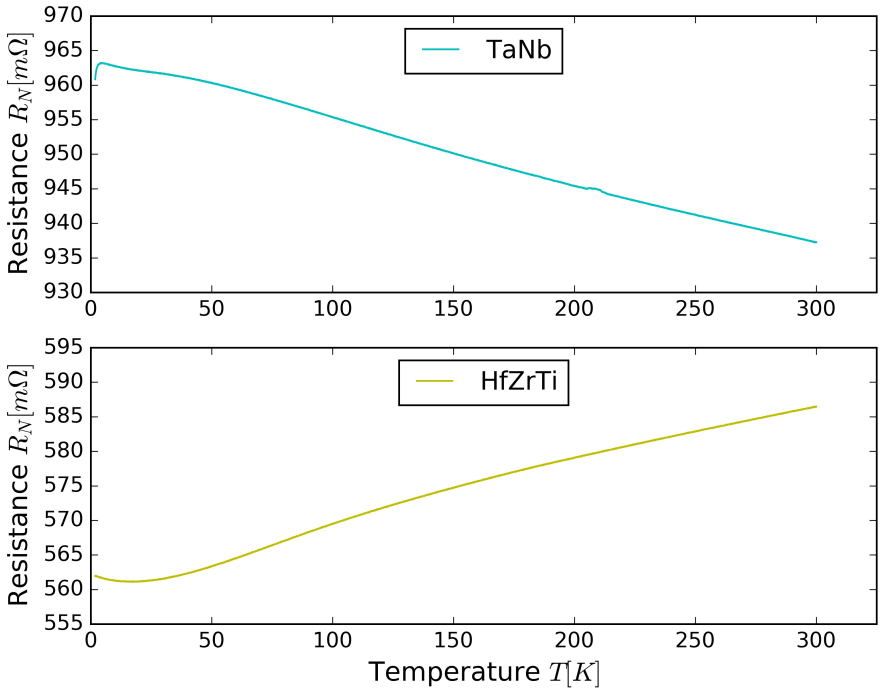

Figure 21: Behaviour of the pure films at low temperature, to clearly see the trends only lines and not measured points are shown. The upper plot shows the resistance of a pure TaNb film. By lowering the temperature the resistivity first increases but right above 1.9K it seems to undergo a superconducting transition. In contrast, in the lower plot for HfZrTi the behaviour seems to be the opposite.

4.2 Transition temperature

The transition temperature can be easily estimated by looking at the graph (Figure 22) of resistivity versus temperature. It is the temperature where the resistivity drops to zero. There are different ways to do this more accurately. In this thesis quite a simple way was chosen by plotting a horizontal line at half of the resistivity right above the transition (50%-method) and then finding the temperature where the resistivity crosses this line. This was done for all compositions and in all possible magnetic fields where the transition still occurred above 1.9K. Figure 22 shows an example of such a determination of the transition temperature.

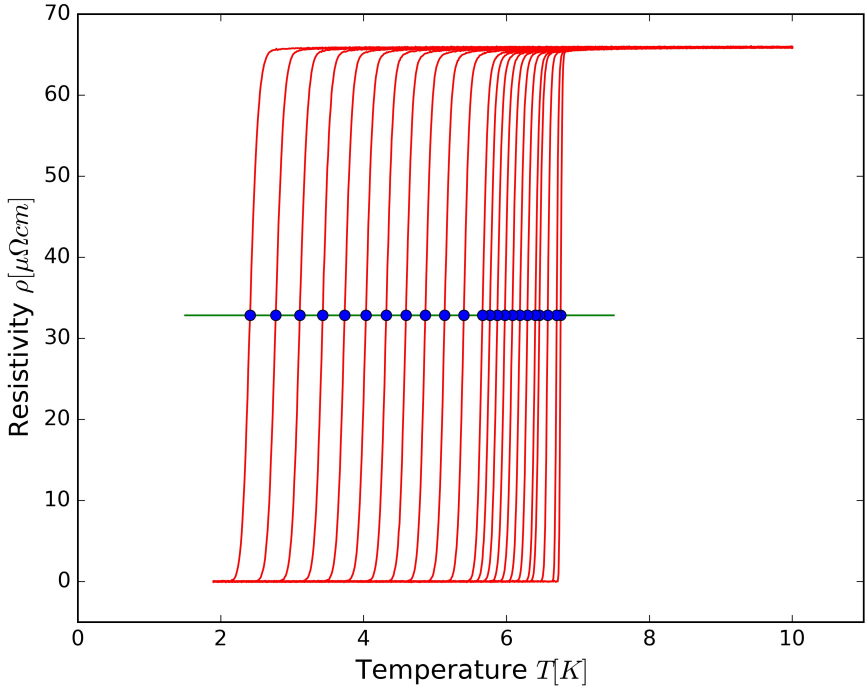

Figure 22: Determination of the transition temperature in different magnetic fields, here for the film with $x = 0.5$. The red lines show the measured resistivity in the different magnetic fields from 0T to 7.5T with a clearly visible superconducting transition. The green line is drawn at half of the resistivity in the normal state at 7K. Indicated by the blue dots are the intersections of the green line with the measured red lines. The x-component (temperature) of these points is then interpreted as the transition temperature.

An even more accurate way would have been to fit the transition curves with the suitable function that includes the critical temperature T_c as fitting parameter. The transitions from the normal to the superconducting state are not completely sharp, they are smeared out. This is because of the superconducting fluctuations which we have to take into account. The resistivity in the normal state is then given by:

$$\rho(T) = \frac{1}{\sigma_N + \sigma'} \tag{4.3}$$

where σ_N is the normal state conductance and σ' the conductance coming from the fluctuations. These fluctuations depend on the dimensions of the films and increase by approaching the transition. For a sample with length l, width w and thickness d larger than the coherence length ξ, i.e. the 3D case, the additional conductance can be estimated by [30]:

$$\sigma' = \frac{e^2}{32\hbar\xi(0)} \left(\frac{T_c}{T - T_c} \right)^{1/2} \tag{4.4}$$

Which leads to the following formula for the normal state resistance:

$$R_{3D}(T) = \frac{R_N}{1 + a_{3D}\left(\frac{T_c}{T - T_c}\right)^{1/2}} \tag{4.5}$$

where $a_{3D} = \frac{R_N w d e^2}{32\hbar l \xi(0)}$.

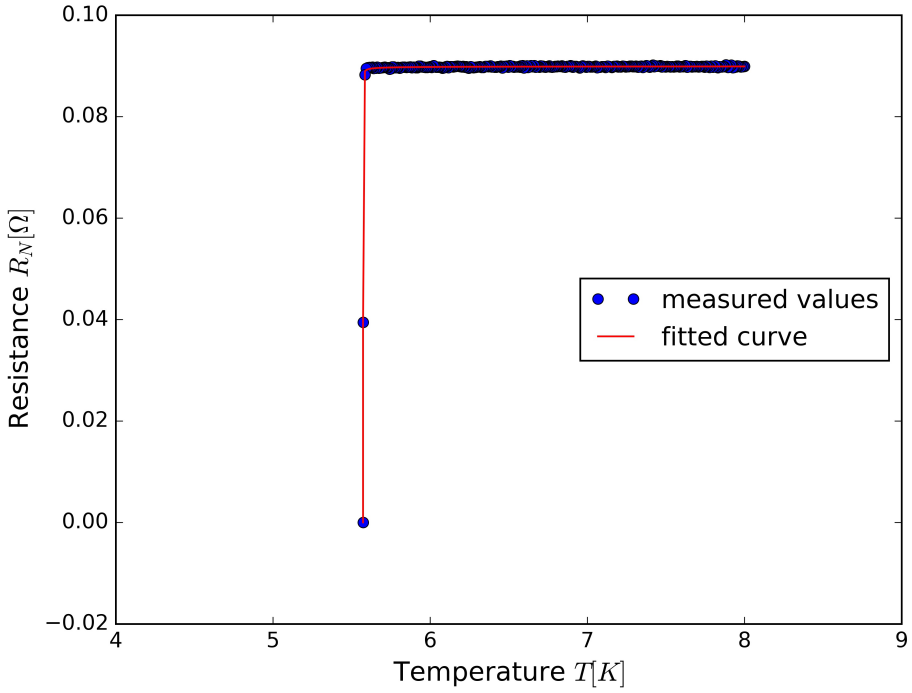

Figure 23: Determination of the transition temperature using the fitting method. The blue dots show the measured resistance in zero magnetic field and the red line shows the least square fit using equation 4.5.

Using R_N, a_{3D} and T_c as fitting parameter, the curves for zero magnetic field were fitted with a least square fit (Figure 23). As expected from the quite sharp transitions the results were nearly the same (with a deviation $< 1\%$) as with the method described above. Furthermore, this method is only applicable in zero magnetic fields as for transitions in magnetic field no simple analytic formula for the fit can be found. So the presented results are the ones from the 50%-method.

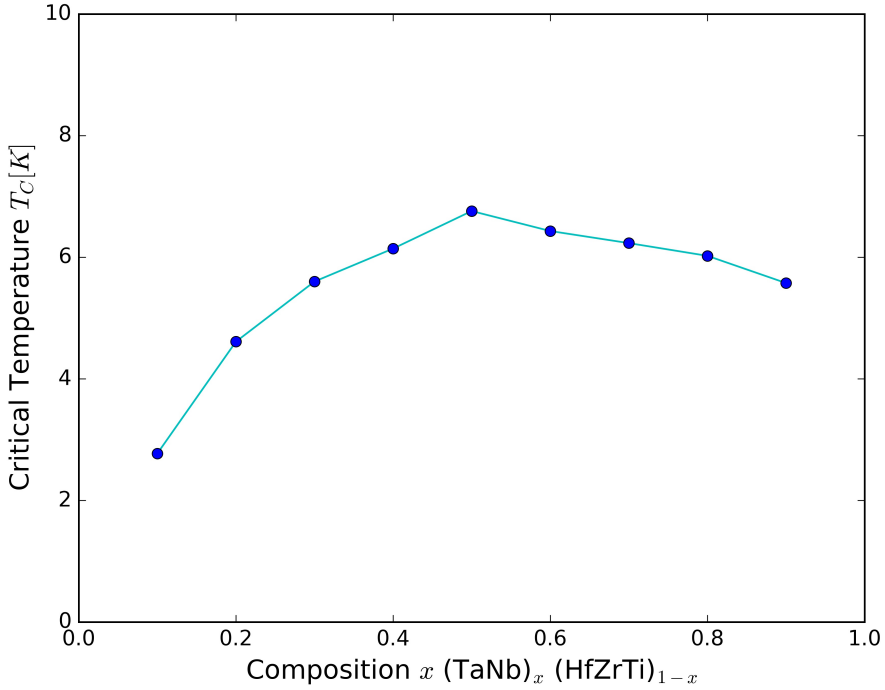

Figure 24: Critical temperature in zero magnetic field for the different compositions. In this and all following plots the dark blue dots show the determined value for the specific parameters and the light blue line is drawn for better understanding of the trend.

The transition temperature is highest for the composition where both target materials have equal parts ($x = 0.5$) and slightly varies for the different compositions as shown in Figure 24. It can further be seen that for the film where there is more than half of HfZrTi, the transition temperature decreases much faster than on the other half with more TaNb.

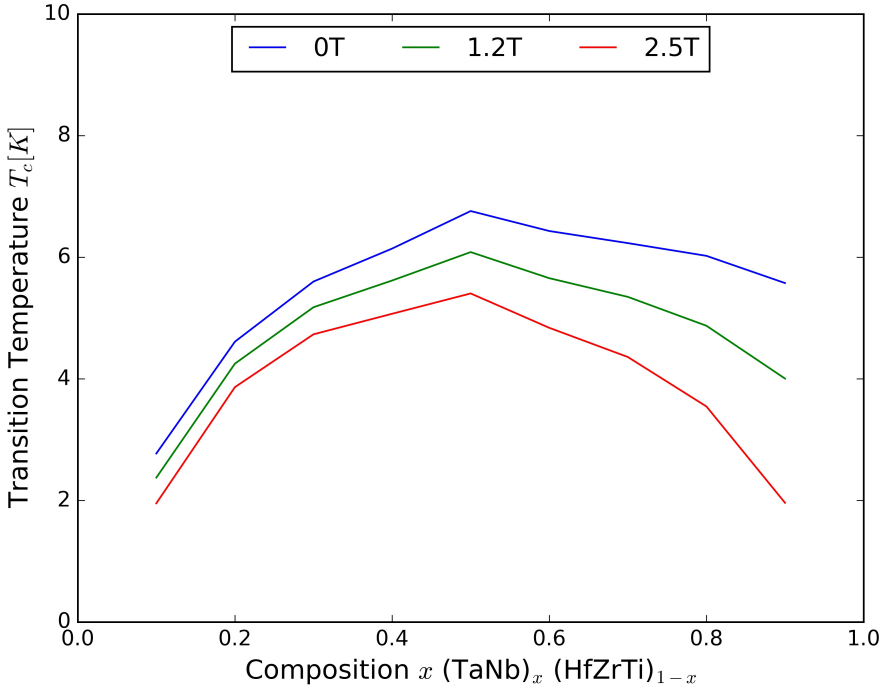

Figure 25: Behaviour of the transition temperature depending on the composition and the magnetic field. To illustrate the influence of the magnetic field on the transition temperature for the different compositions, for each magnetic field from 0T to 2.5T the transition temperature is drawn as a line depending on the composition. The distance between the line is proportional to the slope of the upper critical field dB_{c_2}/dT_c. This means the slope will be higher for composition with larger x then for them with smaller, as also shown in Figure 26.

Figure 25 shows how the transition temperature is lowered in higher magnetic fields. Further, it can be seen that for a fixed composition the transition temperature scales linearly with the magnetic field but not coherently for all the different films. This means that the slope $\frac{dB_{c_2}}{dT_c}$ is different depending on the composition (Figure 26) which will also lead to different critical fields.

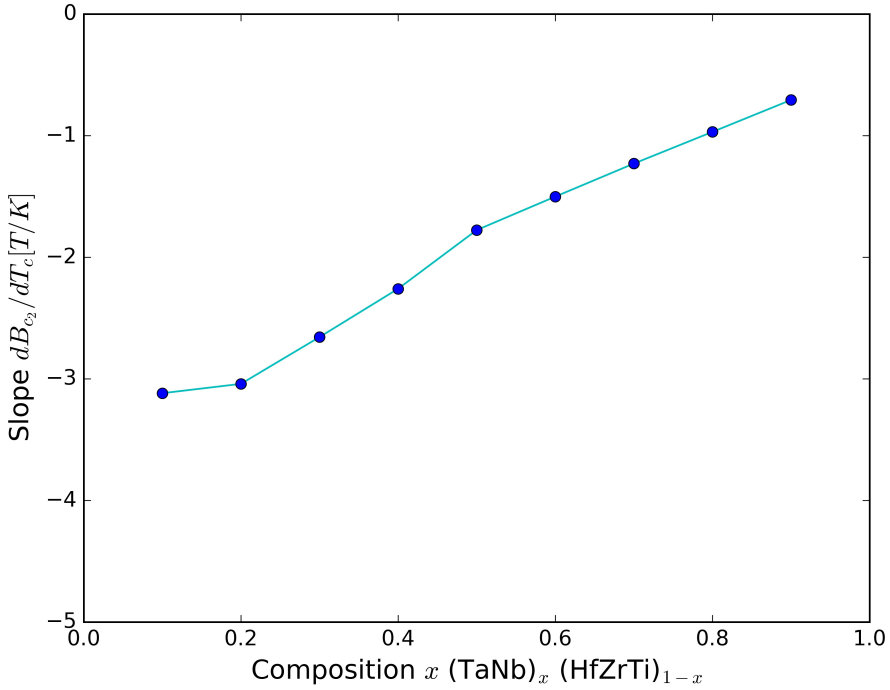

Figure 26: Comparison of the slope of the magnetic field vs. the transition temperature depending on the composition

4.3 Critical field

For the calculation of the critical field at zero temperature, the transition temperatures depending on the different applied fields were plotted against the magnetic field. They show a linear dependence and therefore were linearly extrapolated to zero temperature. This linear fit represents more or less the critical field depending on the temperature $B_{c_2}(T)$. The critical field at zero temperature is then the field where the transition temperature would be 0K and can therefore be interpreted as the intercept on the y-axis in Figure 27.
From the Werthamer, Helfand and Honenberg (WHH) theory [31], the upper critical field at zero temperature in the dirty limit where the mean free path $l << \xi_0$ is given by:

$$B_{c_2} = -0.69 T_c \frac{dB}{dT}\Big|_{T=T_c} \tag{4.6}$$

Using this equation for the extrapolation to zero temperature, the critical field would be lower by approximately a factor of $\frac{1}{\sqrt{2}}$ compared to the results obtained from the linear extrapolation.

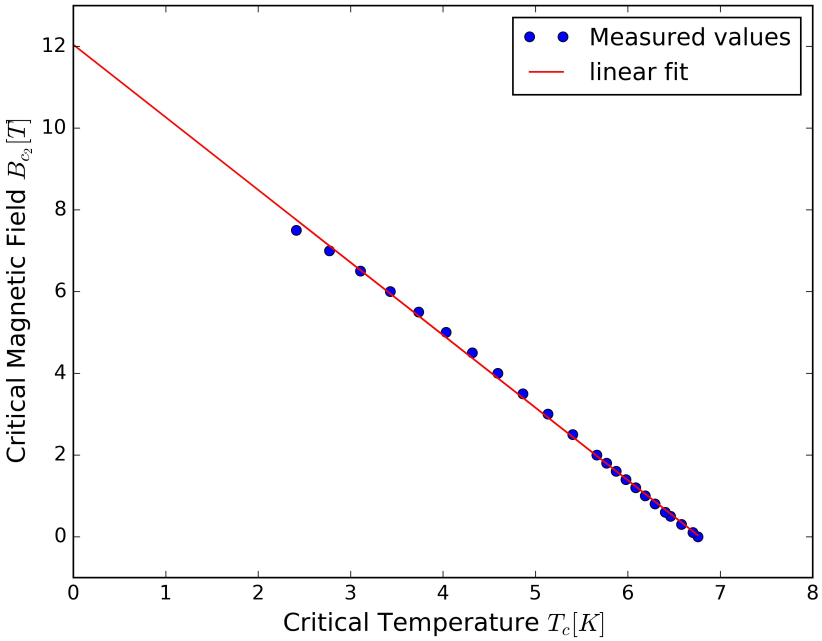

Figure 27: Determination of the upper critical field $Bc_2(0)$ on the example of the composition with equal parts $x = 0.5$. The blue dots are the measured values which are more or less on a line. For the extrapolation to zero temperature a linear fit was done (shown as red line). The intercept of this line determines the magnitude of the upper critical field.

The dependence of the critical field on the composition is shown in Figure 28. It has a maximum for the composition with 30% of TaNb and decreases quite fast on both sides. The minimum can be found in the film with 90% of TaNb with quite a low critical field of around 4T.

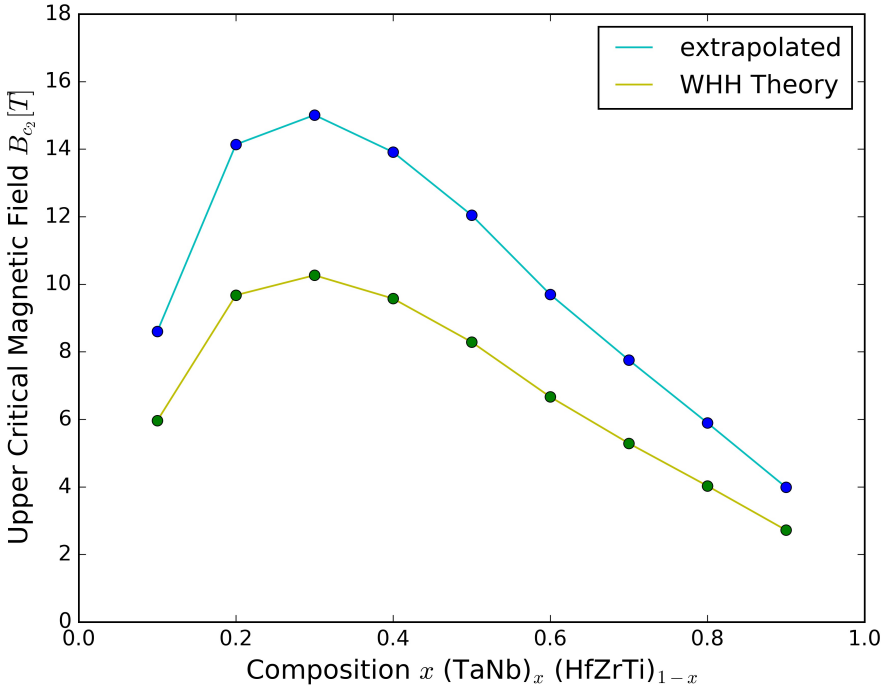

Figure 28: The upper critical field B_{c_2} depending on the composition. The blue dots and line show the extrapolated values of the upper critical field with the method explained above. For the green dots the WHH approximation was used to correct the extrapolated values.

4.4 Coherence length

Equation 2.31 for the upper critical field in the Ginzburg-Landau theory can be solved for the coherence length:

$$\xi_{GL} = \sqrt{\frac{\phi_0}{2\pi B_{c_2}(0)}} \tag{4.7}$$

With this equation the coherence length was calculated using the upper critical fields from WHH theory and plotted in Figure 29.

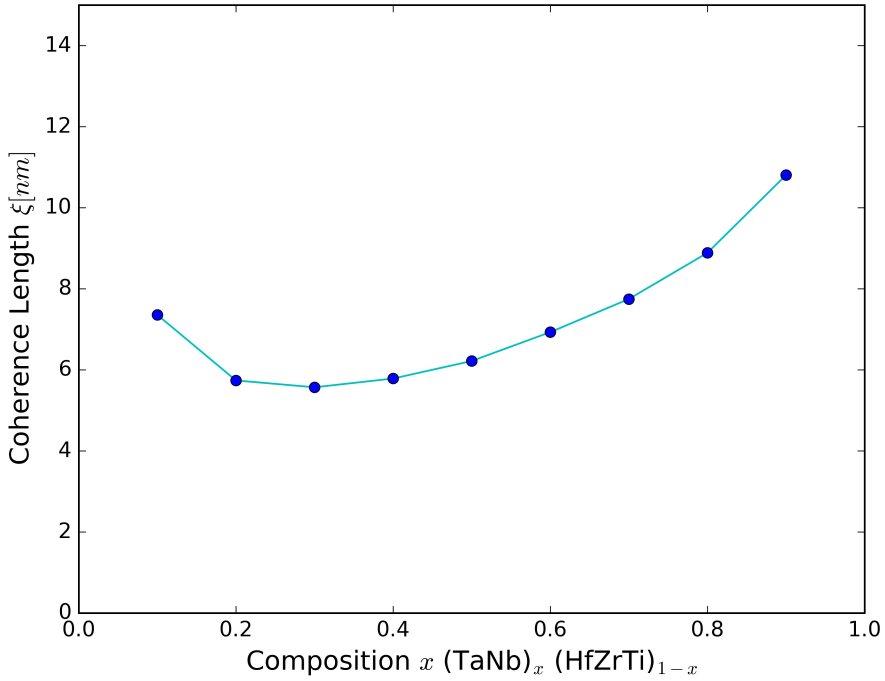

Figure 29: Graph of the coherence length depending on the composition

As the Ginzburg-Landau coherence length is proportional to $\frac{1}{\sqrt{B_{c_2}}}$, it has its minimum of around 5nm where the critical field was maximal at $x = 0.3$ and increases on both sides in a similar way with a maximum at $x = 0.9$ and a value of around 11nm.

4.5 Penetration depth

The penetration depth is a measure of how far a magnetic field can enter a superconductor and depends on the London penetration depth shown in Section 2.2.2. This determination is not as trivial as the ones before as in the equation 2.13 for the London penetration depth parameters as the renormalized mass m^* are included. In the limit of pure superconductors we have $\lambda = \lambda_L$ but for the dirty limit ($l >> \xi_0$) in thin films we get [32]:

$$\lambda(0) = \lambda_L(0)\sqrt{\frac{\xi_0}{l}} \tag{4.8}$$

We can find for the London penetration depth $\lambda_L(0)^2 = \frac{3}{\mu_0 e^2 v_F^2 N(0)}$ by using the following equations for the different parameters of the BCS theory [33]:

$$\xi_0 = \frac{\hbar v_F}{\pi \Delta(0)} \quad \text{and} \quad N(0) = \frac{1}{e^2 \rho_N D} \tag{4.9}$$

and the diffusion constant $D = \frac{1}{3} v_F l$. Putting these equations together we get the formula for the penetration depth [34]:

$$\lambda(0) = \sqrt{\frac{\hbar \rho_N}{\pi \Delta(0) \mu_0}} \tag{4.10}$$

We have already seen the temperature dependence in equation 2.14 as

$$\lambda(T) = \frac{\lambda(0)}{\sqrt{1 - \left(\frac{T}{T_c}\right)^4}} \tag{4.11}$$

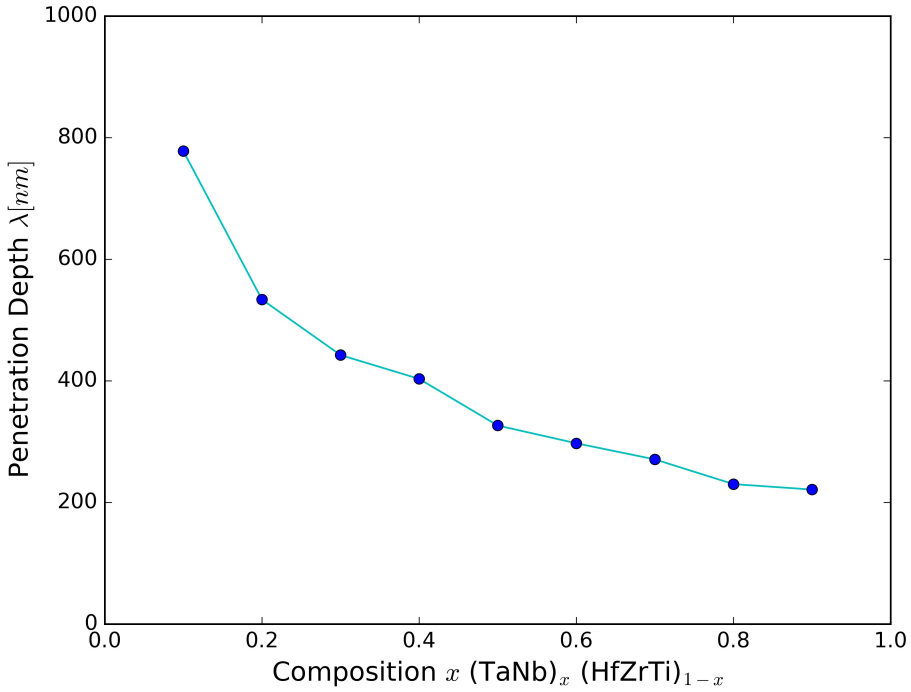

Figure 30: Penetration depth λ depending on the composition

In Figure 30 we see that the penetration depth decreases with increasing fraction of TaNb. The maximum is found for 10% of TaNb with a penetration depth of 800nm. Then, it first decreases quite fast and then slower down to 200nm at 90% of TaNb.

4.6 Further superconducting parameters

From the data some more parameters were calculated. Mostly using the BCS-Theory which is not completely applicable to this material but can be taken as quite a good approximation for unconventional superconductors.

4.6.1 Energy Gap

The energy gap in the BCS-Theory is defined as [34]:

$$\Delta(0) = 1.764 k_B T_c \tag{4.12}$$

and is shown in Figure 31 for the different compositions.

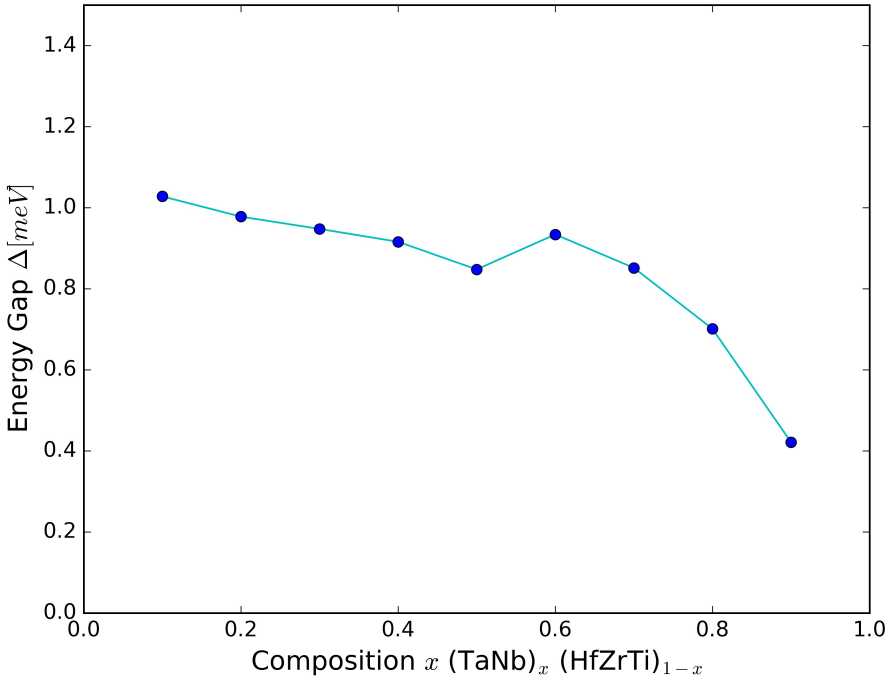

Figure 31: Energy gap calculated from BCS-Theory depending on the composition

The gap in a superconductor can in some applications be seen as a measure for the stability of the superconducting state, for example the critical current increases with increasing gap. As shown in Figure 31, the gap is more or less constant respectively very slightly decreasing between 10% and 70% of TaNb with a value between 0.8meV and 1.0meV. Above 70% TaNb, it starts to decrease sharply down to a value of 0.4meV.

4.6.2 Diffusion constant

As already seen, the electronic diffusion constant is defined as $D = \frac{1}{3} v_F l$ where l is the mean free path. For type II superconductors we can find a formula for the diffusion constant depending on the upper critical field by using the Ginzburg-Landau coherence length. Using again the dirty limit [35], the coherence length near the transition temperature can be written as:

$$\xi(T)^2 = \frac{\pi^3}{24 e^\gamma} l \xi_0 \left(\frac{T_c - T}{T_c} \right)^{-1} = D \frac{\pi \hbar}{8 k_B (T_c - T)} \tag{4.13}$$

with a different definition of the BCS coherence length $\xi_0 = \frac{e^\gamma \hbar v_F}{\pi^2 k_B T_c}$. We then have the equation for the magnetic field depending on temperature as:

$$B_{c_2} = \frac{\hbar}{2e\xi(T)} = \frac{4k_B(T_c - T)}{De\pi} \tag{4.14}$$

taking now the derivative at T_c we arrive at the following relation:

$$\frac{dB_{c_2}}{dT}\Big|_{T=T_c} = -\frac{4k_B}{De\pi} \tag{4.15}$$

which can easily be solved for the diffusion constant:

$$D = -\frac{4k_B}{e\pi}\left(\frac{dB_{c_2}}{dT}\Big|_{T=T_c}\right)^{-1} \tag{4.16}$$

The results are presented in Figure 32.

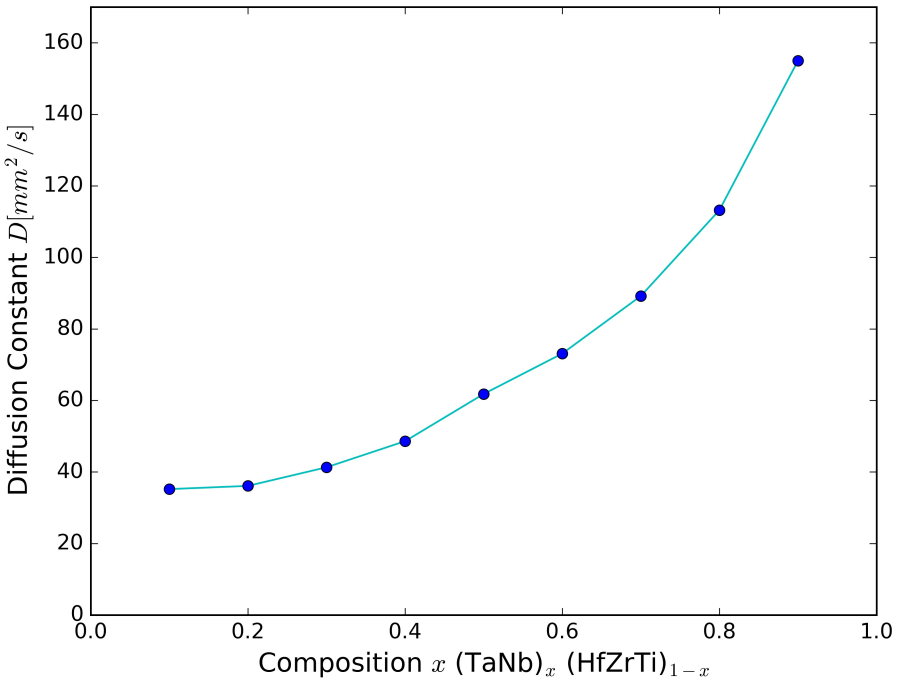

Figure 32: Diffusion constant depending on the composition of the films

From the results we can see that the diffusion constant increases like a parabola for higher fractions of TaNb. From a minimum of around 40mm^2/s to nearly 160mm^2/s.

4.6.3 Density of States at Fermi Surface

Another interesting superconducting parameter is the density of states at the Fermi surface. For the determination we can use the equation we have already seen in Section 4.5 on the penetration depth:

$$N(0) = \frac{1}{e^2 \rho_N D} \tag{4.17}$$

Again, the results are plotted against the composition.

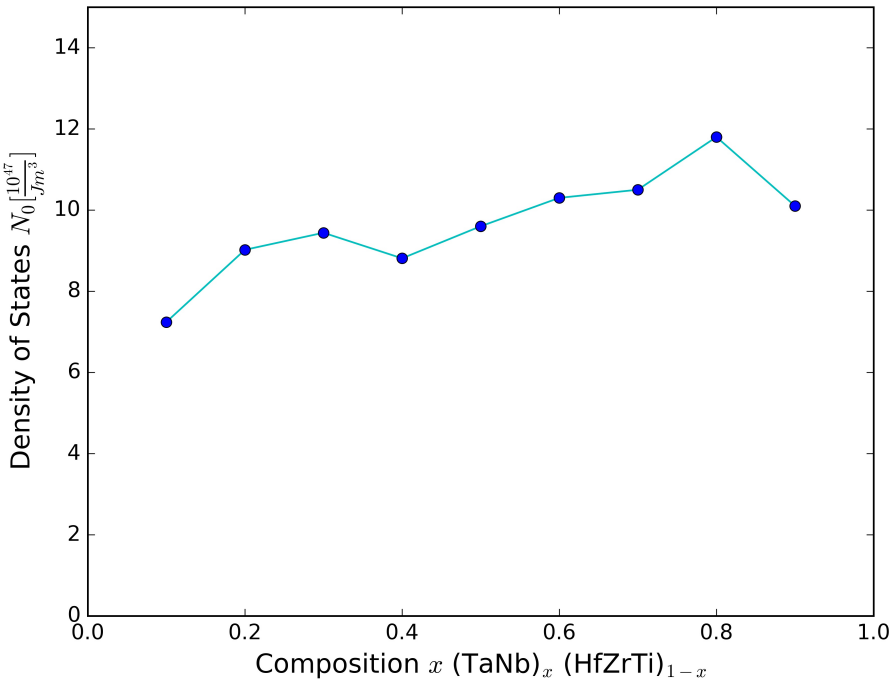

Figure 33: Density of states depending on the composition

The DOS shows approximatively a linear increasing trend for increasing ratio of TaNb (Figure 33) but has some values varying from this linear trend.

4.6.4 Ginzburg Landau Parameter κ

The dimensionless Ginzburg Landau parameter gives some information about how strong type I or II the superconductivity is. Too high values of it can make the superconducting phase unstable. As seen in section 2.2.2, Kappa is defined as:

$$\kappa = \frac{\lambda}{\xi} \tag{4.18}$$

Shown in Figure 34, Kappa decreases linearly for increasing fraction of TaNb with a maximum value of 110 down to a minimum of around 20. So clearly all of these compositions are strong type II superconductors up to really strong type II in the compositions with $x < 0.3$.

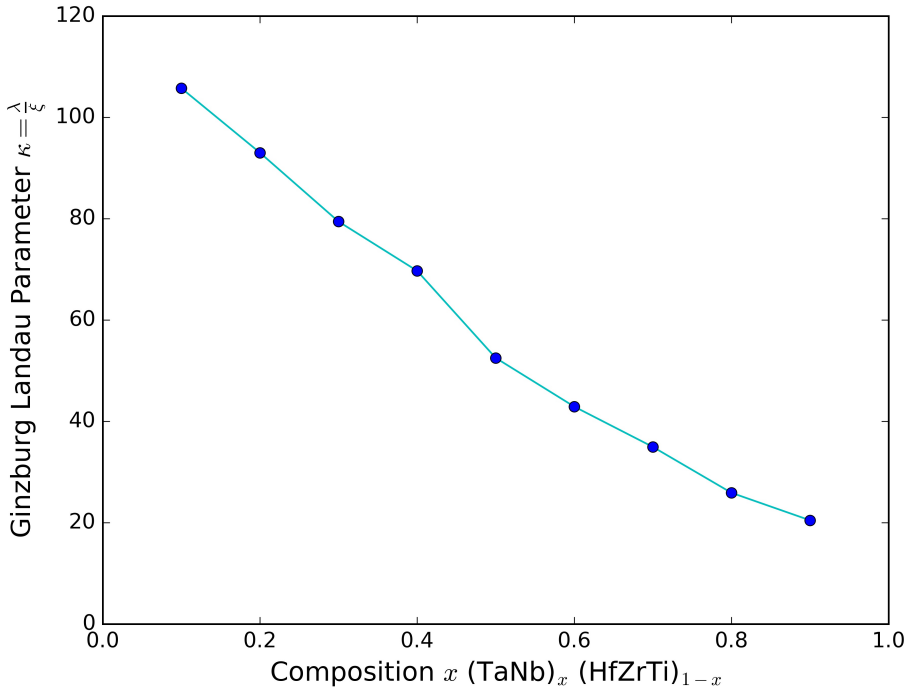

Figure 34: Dimensionless parameter kappa helping to classify between type I and type II depending on the composition

5 Conclusion and Outlook

5.1 Conclusion

In summary, all films $(TaNb)_x(HfZrTi)_{1-x}$ with $0.1 \leq x \leq 0.9$ are superconducting with transition temperatures between 2.5K and 7K. The highest transition temperature is found for $x = 0.5$ with $T_c = 6.76$K. But not for all parameters the composition with $x = 0.5$ seems to be the best. For the upper critical field which is also important for applications, the composition with $x = 0.3$ provides the highest value of $B_{c_2} = 10.3$T. The penetration depth, which is an indicator for how far an external magnetic field can enter the sample, shows a constantly decreasing behaviour for larger fraction of TaNb. So the films with higher x would be favourable. The energy gap calculated from BCS is similar for all composition except from the two with highest part of TaNb where it decreases. A further interesting parameter to mention is the Ginzburg Landau parameter κ which clearly classifies all films as unconventional type II superconductors. The κ is linearly decreasing for higher fractions of TaNb. There were some further parameter examined but they did not show really interesting behaviours.
To conclude there is no overall film composition which could be classified as the best for all applications, as not for all applications the same parameters are important, so the favourable compositions depends on the applications. But we can clearly say that the composition with similar fractions of TaNb and HfZrTi, i.e. x in the range from 0.3 to 0.7, show a more interesting behaviour for further applications than the others.

5.2 Outlook

It could be interesting to do some more measurements on these films. On the one hand, using the exact measured compositions instead of the ones calculated from the sputtering rate and on the other hand, also using exactly squared sheets instead of calculating the sheet resistance from four point measurements afterwards. Also, lowering the film thickness to a few nanometers, which would make them nearly a 2D system, could be worth a try.
As the transition temperature does not only depend on the materials a film consists off but also on the condition during the composition, it could be interesting to vary them. One possibility is to change the substrate temperature during the deposition of the films. Increasing the temperature could also increase the transition temperature. Other possibilities would be to change the process gas or the pressure for the deposition.

Furthermore, in the measurements for the compositions $x = 0.7, 0.8$ an interesting phenomena can be observed. There seems to be a second drop in the resistivity slightly above the transition temperature in higher magnetic fields as shown in Figure 35. By measuring the films again, one could find out if this was a measurement error or a special behaviour of these films.

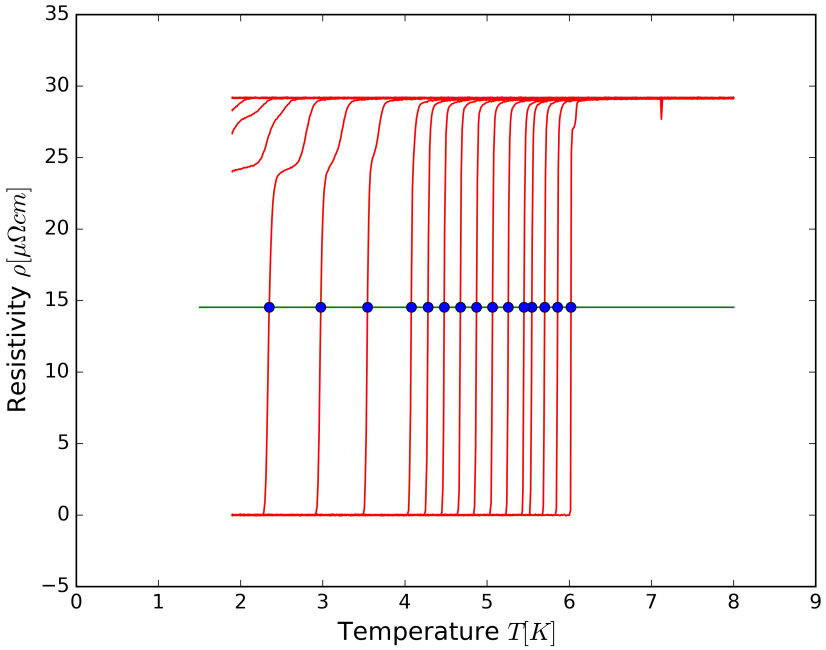

Figure 35: Resistivity in different magnetic fields for the composition of $x = 0.8$. The plot shows two special effects or measurement errors. First, there seems to be a double transition for magnetic fields above 2T, Second, around 7K there is a small drop of the resistivity in the magnetic field of 7.5T.

As seen in [1], the superconductivity in the $(\mathrm{TaNb})_x(\mathrm{HfZrTi})_{1-x}$ crystal is very robust against pressure until the crystal breaks. So it would be interesting to further examine the amorphous films at high pressures to check if this robustness still exists or can even be improved.

A last idea could be to try to even enhance the entropy of the high entropy alloy by either replacing one of the materials in these films or by adding more materials to have an alloy with more than five elements. With this new film one could also do first measurements to find out if they are superconducting and afterwards also the superconducting parameters and the behaviour if pressure is applied.

List of Figures

List of Tables

References

[1] Jing Guo, Honghong Wang, Fabian von Rohr, Zhe Wang, Shu Cai, Yazhou Zhou, Ke Yang, Aiguo Li, Sheng Jiang, Qi Wu, Robert J. Cava, and Liling Sun. Robust zero resistance in a superconducting high-entropy alloy at pressures up to 190 gpa. *PNAS*, 2017.

[2] Chris Woodford. Alloys, June 2018. https://www.explainthatstuff.com/alloys.html. Accessed: 28.11.2018.

[3] J.W. Yeh B.S. Murty, S. Ranganathan. *High-Entropy Alloys*. Elsevier, 2014.

[4] T. S. Smith and J. G. Daunt. Some properties of superconductors below 1°k. iii. zr, hf, cd, and ti. *Phys. Rev.*, 88:1172–1176, Dec 1952.

[5] J.R. Rairden and C.A. Neugebauer. Critical temperature of niobium and tantalum films. *Proceedings of the IEEE*, 52:1234 – 1238, 11 1964.

[6] P. Koželj, S. Vrtnik, A. Jelen, S. Jazbec, Z. Jagličić, S. Maiti, M. Feuerbacher, W. Steurer, and J. Dolinšek. Discovery of a superconducting high-entropy alloy. *Phys. Rev. Lett.*, 113:107001, Sep 2014.

[7] Fabian von Rohr, Michał J. Winiarski, Jing Tao, Tomasz Klimczuk, and Robert Joseph Cava. Effect of electron count and chemical complexity in the ta-nb-hf-zr-ti high-entropy alloy superconductor. *Proceedings of the National Academy of Sciences*, 113(46):E7144–E7150, 2016.

[8] A.V. Narlikar. *Superconductors*. Oxford University Press, 2014.

[9] R. Kleiner W. Buckel. *Superconductivity. Fundamentals and Applications*. WILEY-VCH Verlag GmbH & Co. KGaA, Weinheim, 2004.

[10] T. Neupert. Lecture notes: Introduction to condensed matter theory. University of Zurich, May 2018.

[11] J. Chang. Lecture notes: Condensed matter physics. University of Zurich, 2018.

[12] M. Sigrist. Introduction to unconventional superconductivity. ETH Zurich.

[13] C.L. Henley. Lecture notes on superconductivity. bcs theory. Cornell University.

[14] Nur Haleeda, M Awang Kechik, and R.Abd-Shukor . Effect of yb2o3 nanoparticle addition on superconducting properties of bscco (2223)/ag tapes by acetate precipitation method. 2016.

[15] J. Bardeen, L. N. Cooper, and J. R. Schrieffer. Theory of superconductivity. *Phys. Rev.*, 108:1175–1204, Dec 1957.

[16] University of Cambridge. Superconductivity, 2008. https://www.doitpoms.ac.uk/tlplib/superconductivity/type.php. Accessed: 10.12.2018.

[17] A. Engel. *Vortex Dynamics and Superconducting Phase Diagrams in Ta_xGe_{1-x}/Ge Multilayers with Coplanar Defects*. PhD thesis, Victoria University of Wellington, August 2001.

[18] Allmystery. online, June 2013. https://www.allmystery.de/themen/gw101973-2. Accessed: 20.01.2019.

[19] Mantis. Hipims. online. https://www.mantisdeposition.com/mantis/latest-technology/hipims.html. Accessed: 07.12.2018.

[20] J. Böhlmark. *Fundamentals of High Power Impulse Magnetron Sputtering*. PhD thesis, Institute of Technology. Linköping University, 2005.

[21] AdNaNoTek Corporation. Uhv magnetron sputtering system (mds). online, 2014. http://www.adnano-tek.com/magnetron-sputtering-deposition-msd.html. Accessed: 19.01.2019.

[22] ETH Zurich. Equipment & services. webpage. http://www.first.ethz.ch/equipment/first-equipment/magnetron-sputtering.html, Accessed: 07.12.2018.

[23] Integrated Nanosystems Research Facility. Dektak 3 profilometer. online. http://www.inrf.uci.edu/facility/equipment/characterization/dektak-3-profilometer/. Accessed: 19.01.2019.

[24] Quantum Design. Physical property measurement system. Webpage with Brochures. https://www.qdusa.com/products/ppms.html. Accessed: 10.12.2018.

[25] A. Gafner. *Construction of NMR equipment to be used in the Physical Properties Measurement System (PPMS, Quantum Design)*. PhD thesis, University of Zurich, June 2006.

[26] LOT-QuantumDesign AG. System zur messung physikalischer eigenschaften (ppms). https://lot-qd.ch/de/produkte/materialwissenschaften/systeme-zur-messung-physikalischer-eigenschaften/product/system-zur-messung-physikalischer-eigenschaften-ppms/. Accessed: 10.12.2018.

[27] Quantum Design. *Physical Property Measurement System. Hardware Manual*, February 2008.

[28] LOT-QuantumDesign AG. *PPMS Physical Property Measurement System*.

[29] Michael Heaney. *Electrical Conductivity and Resistivity*, pages 7–1 to 7. 01 2003.

[30] X. Zhang. *Characteristics of Tungsten Silicide and its Application for Single X-ray Photon Detection*. PhD thesis, University of Zurich, 2018.

[31] Y. Chen J.L. Zhang, L. Jiao and H.Q. Yuan. Universal behavior of the upper critical field in iron-based superconductors. *Frontiers of Physics*, 6(4):463–473, December 2011.

[32] M. Tinkham. *Introduction to Superconductivity*. Dover Publications, INC., 2 edition, 2004. pages: 104ff.

[33] Xiaofu Zhang, Andreas Engel, Qiang Wang, Andreas Schilling, Alexey Semenov, Mariia Sidorova, Ilya Charaev, Konstantin Ilin, and Michael Siegel. Characteristics of superconducting tungsten silicide wxsi1-x for single photon detection. *Physical Review B*, 94, 07 2016.

[34] M. Mondal. *Phase fluctuations in a conventional s-wave superconductor: Role of dimensionality and disorder*. PhD thesis, Tata Institute of Fundamental Research, Mumbai, 2013. http://www.tifr.res.in/ superconductivity/pdfs/mintu.pdf.

[35] T. P. Orlando, E. J. McNiff, S. Foner, and M. R. Beasley. Critical fields, pauli paramagnetic limiting, and material parameters of nb_3sn and v_3si. *Phys. Rev. B*, 19:4545–4561, May 1979.